Unraveling the burial and exhumation history of foreland basins using the spread of apatite (U-Th-Sm)/He single grain ages

Kevin A. Frings[1,2], Elco Luijendijk[3], István Dunkl[4], Peter Kukla[5], Nicolas Villamizar-Escalante[2], Herfried Madritsch[6], Christoph von Hagke[2]

[1]Institute for Tectonics and Geodynamics, RWTH Aachen University, Aachen, 52064, Germany
[2]Department of Environment and Biodiversity, Division of Geology & Physical Geography, Salzburg University PLUS, Salzburg, 5020, Austria
[3]Department of Earth Science, University of Bergen, Bergen, 5020, Norway
[4]Geoscience Center, Department of Sedimentology and Environmental Geology, University of Göttingen, Göttingen, 37077, Germany
[5]Geological Institute, RWTH Aachen University, Aachen, 52062, Germany
[6]Nagra, Wettingen, 5430, Switzerland, now at: Swisstopo, Swiss Geological Survey, Seftigenstrasse 264, 3084 Wabern

Correspondence to: Kevin A. Frings (frings@geol.rwth-aachen.de)

Abstract. Reconstructing the evolution of foreland basins that experienced late exhumation is challenging due to an incomplete sedimentary record. Thermochronometry has been applied successfully to reconstruct basin evolution, but the method is subject to uncertainties. For the Swiss Molasse Basin, a wide range of exhumation magnitude and timing has been proposed based on thermochronometry. We aim to reduce uncertainty by dating larger numbers of grains and samples, to obtain statistically more robust data. New apatite (U-Th-Sm)/He (AHe) data from a single borehole shows ages of 4 to 30 Ma in the upper 500 meters and ages of 3 to 80 Ma below 1300 meters. This is counterintuitive as a total reset is expected at depths exceeding approximately 600 m. To arrive at a single consistent thermal history including our and previously published data, we conduct thermal modeling with different software. In particular we test the influence of different provenance histories and distinguish between cooling associated with changes in heat flow vs changes in exhumation.

We determine 1050 m +/- 100 m of exhumation, starting slowly at 13 Ma and accelerating at 9 Ma. Coinciding with exhumation, heat flow begins to rise sharply, causing heating until 5 Ma, despite ongoing exhumation. We show that this discrepancy between start of exhumation and start of cooling is the main reason for differing estimates for the burial and exhumation history of the basin. We suggest that the remaining misfit between modeled and measured Molasse AHe ages can be explained by post-Miocene hydrothermal flux in the Neogene sediment fill above a sealing layer, potentially the Middle Jurassic claystones or Triassic evaporites.

In summary, we show that a single consistent model for basin exhumation relies on large sets of grains and samples, as well as inclusion of provenance ages in the models. With timing of the main exhumation phase constrained to start at 9 Ma, we can rule out a 5 Ma climatic event as exhumation driver. As the region is not affected by extensive faulting, deep seated processes related to mantle dynamics remain as exhumation driving process.

1 Introduction

Constraining the burial and exhumation history of foreland basins is important for a variety of research objectives. First, timing and magnitude of exhumation of foreland basins provides information on the underlying processes, in particular the respective influence of climate, tectonics, or mantle dynamics (e.g., Bernet and Spiegel, 2004; Malusà et al., 2005; Glotzbach et al., 2011a; von Hagke et al., 2012; François et al., 2014; Lacombe et al., 2019; Stalder et al., 2020).

40 Furthermore, foreland basins are witnesses of the tectonic history of the orogen in their hinterland (e.g., Brewer et al., 2003; Bernet et al., 2009; Glotzbach et al., 2011b; Anfinson et al., 2020). Third, foreland basins may contain hydrocarbon resources (e.g., Beaumont and Bout, 1985; Beydoun et al., 1992; Gusterhuber et al., 2014), can potentially be targets for geothermal energy production (e.g., Wolfgramm et al., 2007; Moeck et al., 2015), or offer potential sites for radioactive waste disposal within suitable rock units (e.g., Nagra, 2014).

The most powerful tool to recover foreland basin evolution is stratigraphy. However, the stratigraphic record may be incomplete due to late-stage basin exhumation, as has for instance been reported from the foreland basins of the southern central Andes (Levina et al., 2014), the Zagros fold-and-thrust belt and foreland basin (Koshnaw et al., 2017), or the Molasse Basin of the European Alps (Cederbom et al., 2004; Willett and Schlunegger, 2010; Cederbom et al., 2011; Schlunegger and

50 Mosar, 2011). In these cases, low-temperature thermochronometry can be used to recover foreland basin evolution (e.g., Mazurek et al., 2006; van der Beek et al., 2006; Cederbom et al., 2011; von Hagke et al., 2012; Folguera et al., 2015). This method is particularly useful, as it provides insights on landscape evolution including relief development through time (Ehlers and Farley, 2003; Braun et al., 2012; Glotzbach et al., 2011a; Valla et al., 2012), tectonic processes acting on basin or orogen scale, as well as the activity of individual faults (Ehlers and Farley, 2003; Reiners and Brandon, 2006; Fitzgerald

55 et al., 2009; Mock et al., 2020; von Eynatten et al., 2020). Furthermore, low-temperature thermochronometry can be used to constrain fluid flow and timing of activity of thermal springs on local or regional scale (Louis et al., 2019). In addition to in situ thermochronometry, detrital thermochronometry can be used to investigate thermal histories of basins and their source regions (Bernet & Spiegel, 2004; Spiegel et al., 2004; Luijendijk et al., 2011; Tatzel et al., 2017). Commonly, detrital low-temperature thermochronological data shows a spread in single grain ages from a given sample (Brown et al., 2013; Green

60 and Duddy, 2018; Fox et al., 2019). This can be exploited, for instance, by determining different single grain age populations in fission track data and deriving individual time temperature histories (e.g., Fillon et al., 2013; Cecil et al., 2014; Fox and Shuster, 2014). However, confounding factors exist that make data interpretation challenging, such as unconstrained kinetics, crystal zonation or unknown inherited ages (Flowers et al., 2009; Ault and Flowers, 2012; Cecil et al., 2014; Djimbi et al., 2015; Fox et al., 2019). This is particularly the case for (U-Th-Sm)/He dating where multiple factors may lead to an

65 age spread that is independent of basin exhumation (Brown et al., 2013; Green and Duddy, 2018; Fox et al., 2019). In this

contribution we present an extensive detrital apatite (U-Th-Sm)/He data set from a key location in the foreland basin of the Central European Alps. Using established and new thermal modeling techniques, we show that the spread in singe grain ages in this data set can be used to reconcile different hypotheses proposed for exhumation of the alpine foreland.

2 Geological setting and conflicting hypotheses

70   The Swiss Molasse Basin, i.e. the northern foreland basin of the Central European Alps (Fig. 1) has been studied intensely, including the link between alpine mountain building and foreland basin evolution (Sinclair and Allen, 1992; Schmid et al., 1996; Sinclair, 1997; Mosar, 1999; Pfiffner et al., 2002; Schmid et al., 2004; Bousquet et al., 2008; Handy et al., 2010; Willett and Schlunegger, 2010; von Hagke et al., 2012; Hinsch, 2013; Ortner et al., 2015; Schlunegger and Kissling, 2015; Schlunegger and Castelltort, 2016). Likewise, basin stratigraphy is well established (e.g., Kempf et al., 1997; Schlunegger et

75   al., 1997; Kuhlemann and Kempf, 2002; Berger et al., 2005a). Furthermore, it has been shown that the basin experienced Neogene uplift and exhumation (e.g., Schegg and Leu, 1998; Cederbom et al., 2004; Mazurek et al., 2006; Willett and Schlunegger, 2010; Cederbom et al., 2011; Schlunegger and Mosar, 2011; Baran et al. 2014). In order to constrain this late stage history, different methods have been applied, including vitrinite reflectance (Schegg and Leu, 1998; Mazurek et al., 2006), wedge mechanics (Willett and Schlunegger, 2010; Schlunegger and Mosar, 2011; von Hagke et al., 2014a), or low-

80   temperature thermochronometry (Mazurek et al., 2006; Cederbom et al., 2011; von Hagke et al., 2012; von Hagke et al., 2014b; Mock et al., 2020). Studying the northern rim of the basin in close vicinity of the Jura Mountains, Mazurek et al. (2006) argue for 750 m to 1050 m of exhumation starting at 9 Ma, while Cederbom et al. (2011) suggest exhumation of 800 m to 1600 m since approximately 5 Ma. A compilation of existing thermochronological data shows that different scenarios of magnitude and timing of exhumation are possible based on interpretation of existing data, ranging from onset of

85   exhumation as early as 12 Ma to late stage exhumation, commencing at 4 Ma (von Hagke et al., 2015).

In part, these conflicting results may be because thermochronological data is derived from sedimentary samples. Individual grains possibly witnessed a different pre-depositional thermal history, which can affect their fission track annealing and helium retention behavior (Bernet et al., 2001; Fillon et al., 2013; Cecil et al., 2014; Fox and Shuster, 2014). This may

90   particularly be the case for the difference between studies in the proximal Molasse basin, where the Alps form the sediment source (Cederbom et al., 2011; von Hagke et al., 2015; Mock et al., 2020), and the more external parts, where sediments may partly derive from the Black Forest (e.g., Mazurek et al., 2006). We present new apatite (U-Th-Sm)/He thermochronology (AHe) data from the Bülach well (BUL-1, Figs. 1, 2). In this location grains deriving from the Black Forest as well as the Alps are expected, offering the opportunity to cover all populations relevant for interpreting late-stage basin thermal history.

95   The region of the northern Swiss Molasse Basin and, consequently, the sediments sampled in this study have witnessed different tectonic phases, starting after the Variscan orogeny in Permian times. Therefore, we first summarize the pre-Alpine

history of the region, followed by the tectonostratigraphic evolution of the foreland basin and sediment source regions, as well as a summary of the heat flow and geothermal gradient history.
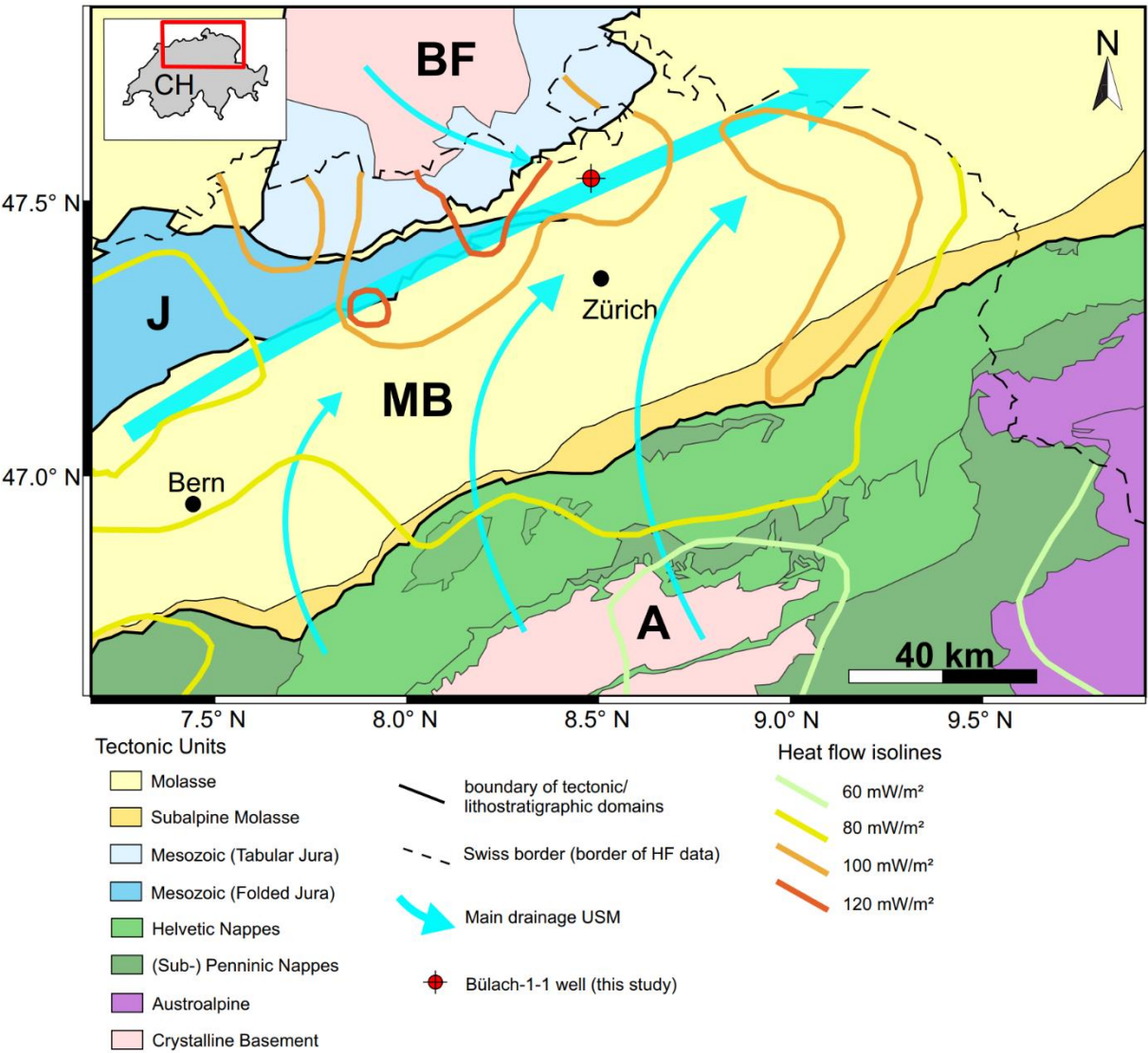
Figure 1. Tectonic map of the study area in northern Switzerland (modified after von Hagke et al., 2012). Relevant domains are shown: BF: Back Forest Massif, A: Alps, J: Jura fold-thrust-belt, MB: Molasse Basin. Drainage directions of the time of USM deposition ~ 22 Ma is indicated (after Kuhlemann & Kempf, 2002). Heat flow isolines indicate recent heat flow (from Sachs & Eberhard based on Medici & Rybach, 1995) Location of the study area (Bülach well) is indicated in red.

2.1 Pre-Alpine history

During the lower Permian, the region underwent post-variscan extension, leading to the formation of graben and half-graben structures in large parts of Europe (Eisbacher et al., 1989; Echtler and Chauvet, 1992; McCann et al., 2008; Geyer et al., 2011). Lower Permian sedimentation is followed by an upper Permian unconformity in the region, as shown by
110   interpretation of seismic profiles (Diebold et al., 1991). Above the unconformity, Triassic to Jurassic passive margin carbonates from an epicontinental marine environment were deposited (Geyer et al., 2011). Tectonic activity during that time is limited, although extensional reactivation of pre-existing faults may have occurred locally in Triassic and Early Jurassic times (Wetzel et al., 2003; Marchant et al., 2005; Roche et al. 2020). Likewise, in the Upper Jurassic sequence, hardgrounds mark episodic erosional phases (Nagra, 2020). Cretaceous passive margin sediments are not preserved in the region (e.g.,
115   Haldimann et al., 2017; Nagra, 2020), but remnants were found in synclines of the Jura Mountains (e.g., Strasser et al., 2016) and farther east in the Molasse basin (e.g., Ortner et al., 2015). The original thickness of these sediments has been estimated based on vitrinite reflectance and apatite fission track data (Schegg and Leu, 1998; Mazurek et al., 2006). Obtained values range from 0 - 200 m (Crampton and Allen, 1995; Schegg and Leu, 1998), to about 500 m (e.g., Mazurek et al., 2006), and even up to 1400 m (Schegg and Leu, 1998). Erosion has been associated with northward migration of the forebulge of the
120   Alpine subduction zone in late Cretaceous to Paleogene times (Crampton and Allen, 1995).

2.2 Tectonostratigraphic evolution of the Central Alps and their northern foreland basin

Following the passive margin setting, subduction of the oceanic part of the European plate under the Adriatic continental plate and the subsequent continent-continent collision after approximately 35 Ma resulted in the formation of the Central
125   Alps (e.g., Schmid et al., 1996). In Eocene times, continent-continent collision started with distal parts of the European margin entering the subduction channel (e.g., Mosar et al., 1996; Stampfli and Marchant, 1997; Cardello et al., 2019). With the collisional phase, formation of a foreland basin started (Pfiffner, 1986; Sinclair et al., 1991; Sinclair, 1997; Burkhard and Sommaruga, 1998; Pfiffner et al., 2002; Schlunegger et al., 2007). At 32 Ma, the Central Alps witness increased erosion (Hurford, 1986; Schmid et al., 1996), possibly linked to slab breakoff (Davies and von Blanckenburg, 1995). In early
130   Miocene times, approximately at 22 - 20 Ma, European passive margin sediments were detached from the underlying European basement, forming the Helvetic cover nappes (Pfiffner, 2011; Herwegh et al., 2020). Buoyancy-driven subvertical uplift of the thickened crust and exhumation of the external crystalline massifs at about 20 Ma has been associated with delamination of lower European crustal units from the lithospheric mantle or rollback of the European Plate (Fry et al., 2010; Glotzbach et al., 2011a; Schlunegger and Kissling, 2015; Egli et al., 2017a; Herwegh et al., 2017; Kissling and Schlunegger,
135   2018; Herwegh et al., 2020).

Eo-Oligocene crustal-scale extension led to the formation of the European Cenozoic Rift System that also affected the northern Alpine foreland (Hinsken et al., 2007; Ziegler, 1992). Opening of the Upper Rhine Graben, a major segment of this rift system, caused uplift of its flanks and subsequent exposure of Mesozoic rocks in the area of the future Black Forest
140 Massif (Fig. 1). Uplift of the area was further enhanced by north-westward migration of the flexural bulge of the northern Alpine foreland through the region in the Early Miocene (Bourgeois et al., 2007; Ziegler and Dèzes, 2007). The sediments derived from this erosion have partly been transported to the Molasse Basin (e.g., Kuhlemann and Kempf, 2002). This includes Mesozoic sediments, as well as stratigraphically lower amphibolite facies ortho- and paragneisses (e.g., Egli et al., 2017b), Carboniferous granitic plutons, and Upper Devonian to Lower Carboniferous metasediments (e.g., Güldenpfennig
145 and Loeschke, 1991; Schaltegger, 2000; Sawatzki and Hann, 2003; Geyer et al., 2011).

This protracted geological history is reflected in the stratigraphy of the Molasse Basin. Sedimentation started with the deposition of flysch sediments, which continued until middle Oligocene times (Sinclair and Allen, 1992). Increased exhumation of the orogen at 32 Ma led to increased sediment discharge into the foreland basins (Sinclair, 1997; Schlunegger
150 and Castelltort, 2016). The following Molasse sedimentation can be separated in two regressive megacycles (Kuhlemann and Kempf, 2002). The lower and upper cycle of the Molasse sediments in this area are subdivided into the Untere Meeres Molasse (UMM. "Lower Marine Molasse", ca. 31.5 – 30 Ma (Kempf et al., 1997; Kempf et al., 1999)), Untere Süßwasser Molasse (USM, "Lower Freshwater Molasse", ca. 30 – 21 Ma, locally until 19 Ma (Kempf et al., 1997; Kempf et al., 1999)), Obere Meeres Molasse (OMM, "Upper Marine Molasse", 21 – 17 Ma (Bolliger, 1999)), and Obere Süßwasser Molasse
155 (OSM, "Upper Freshwater Molasse", 17 – 13 Ma (Kempf et al., 1997; Kempf et al., 1999)) (Matter et al., 1980). Commonly German abbreviations are used in literature. Paleogeographic studies show that sediments of the USM derive from the Central Alps as far as Lake Geneva and from the adjacent Black Forest Massif and the Swabian Alp (Kuhlemann and Kempf, 2002; Berger et al., 2005b). Catchment area maps show that during the Oligocene USM sediments derive from the Helvetic and Flysch units (e.g., Spiegel et al., 2001). In Early Miocene times at around 20 Ma, erosion successively cut into
160 Middle and Upper Penninic units of the Central Alps and reached levels of the Lower Penninic units in Middle Miocene times, including its Subpenninic Basement, the Lepontine Dome (Spiegel et al., 2001).

The southern part of the Molasse basin was affected by thrusting of the Alpine orogen in early Miocene times, shortly after the sediments were deposited (Schlunegger et al., 1997; Kempf et al., 1999). This imbricate stack is called Subalpine
165 Molasse and can also be considered the most external unit of the Helvetics (Ortner et al., 2021). At approximately 14 Ma, deformation of the Jura fold-and-thrust belt started as a result of thin-skinned progradation of the Alpine front into the foreland (Laubscher, 1978; Burkhard and Sommaruga, 1998; Looser et al., 2021). The main phase of folding started after about 12 Ma (Sommaruga et al., 1997; Becker, 2000; Malz et al., 2016). The distal part of the Molasse Basin was barely deformed internally, as the basin got passively transported above the basal detachment of the Jura Mountains (Laubscher,
170 1986). Roughly at the same time, the Central Alps and the Molasse Basin were affected by exhumation (Mazurek et al.,

2006; Bernet et al. 2009; Carrapa et al. 2009; Cederbom et al., 2011; von Hagke et al., 2012; von Hagke et al., 2014b; Schlunegger and Kissling, 2015). Different possible drivers have been suggested for this exhumation, namely climatic changes (Cederbom et al., 2004; Champagnac et al., 2009), tectonic forcing (Burkhard and Sommaruga, 1998; Persaud and Pfiffner, 2004; Reinecker et al., 2008), mantle processes (Schlunegger and Castelltort, 2016), or a combination thereof (e.g.,
175 Cederbom et al., 2011; Schlunegger and Mosar, 2011; von Hagke et al., 2012).

2.3 Thermal history of the Swiss Molasse Basin

Geothermal gradients have been high in the late stages of the Variscan orogeny, with values ranging between 50 and 130 °C/km (Mazurek, 1992, 1998). Heat flow and gradients decreased through the Mesozoic to values around 70 mW/m²,
180 possibly followed by a heating event in late Jurassic to early Cretaceous times (Timar-Geng et al., 2004; Mazurek et al., 2006; Omodeo-Salé et al., 2021; Villagómez Díaz et al., 2021). Peak values proposed are about 90 mW/m² in Early Cretaceous times. Subsequently, heat flow values decreased below 70 mW/m² until Miocene times, with geothermal gradients ranging between 15 °C/km and 30 °C/km (Mazurek et al., 2006; Schegg and Leu, 1998). Following this, Miocene heating is proposed by many models, and heat flow increases to over 100 mW/m² (e.g., Mazurek et al., 2006), peaking in
185 recent times at around 120 mW/m² for the Bülach area (Medici and Rybach, 1995). Post-glacial hydrothermal fluid flow affected the region of the northern Swiss Molasse Basin (Sonney and Vuataz, 2008). This hydrothermal activity results in heat flow anomalies throughout the basin (Fig. 1). One example from the study area is the Baden and Schinznach hydrothermal system (Luijendijk, 2019).

2.4 Structure and stratigraphy of the study area

190

Alpine shortening barely affected the study area. The most prominent structure in the surroundings of the investigated BUL-1 borehole in Bülach is the Baden-Irchel-Herdern Lineament (BIH, Nagra, 2014), roughly one kilometer to the south. It has been interpreted as a Middle Miocene normal fault that was inherited from a Permo-Carboniferous precursor structure, and whose western segment was overprinted by Late Miocene shortening in the Jura fold thrust belt (Diebold, 1989; Malz et al.,
195 2016). The stratigraphy encountered in the BUL-1 well starts with 50 meters of siliciclastic Permian Rotliegend sediments belonging to the Weitenau Formation (Fig. 2). This formation consists mainly of sandstones with thin claystone intercalations and breccias that were deposited in the Constance-Frick Trough (Diebold and Noack, 1997; Madritsch et al., 2018). Lower Permian sediments are capped by the regional upper Permian unconformity. The succession from Lower Triassic to Upper Jurassic strata is completely recovered. 816 meters of Mesozoic deposits were drilled, including Triassic
200 siliciclastic rocks, carbonates and evaporites, while being dominated by Jurassic limestones, claystones and marls in the upper part. The boundary between the Jurassic and Molasse sediments is marked by the two meters thick Siderolithikum, a reddish-brown claystone with abundant iron-pisoids of Eocene age. This borehole section also shows tectonic overprint,

possibly related to a splay thrust of the BIH (Fig. 2; Nagra, 2019). The Molasse section starts with 54 meters of USM I
sandstones, siltstones and silty marls, topped by 448 meters of alternations of silty to sandy marls, sandstones, siltstones and
205 argillaceous marls, resembling the USM II formation. Stratigraphically higher Molasse sediments (OMM and OSM) were
not drilled due to the location of the well in a river valley. However, they are exposed at the surface within a radius of two
kilometers (Haldimann et al., 2017). The top 34 meters of the well comprise Quaternary sandy gravels.
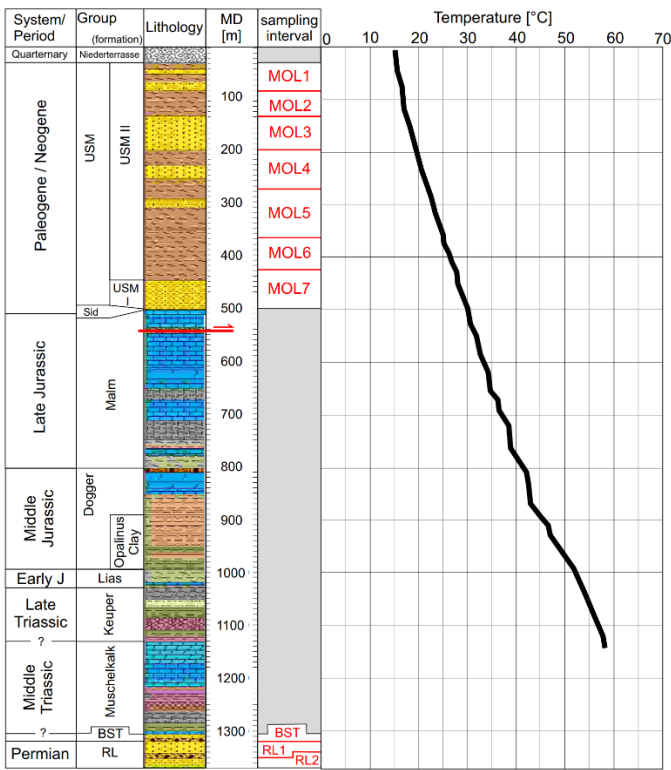
Figure 2. Lithostratigraphic log of the BUL-1 well (modified after Kaehr and Gysi, 2021) and measured borehole temperatures
210 **(Nagra, 2020). Sampling intervals and depth ranges are indicated and named MOL1 – MOL7, BST, RL1 and RL2. Fault at the top**
Mesozoic shown as prognosed in accordance with pre-drilling 3D-seismic interpretations (Nagra, 2019).

3 Methods

3.1 (U-Th-Sm)/He thermochronology, sampling and measurements

To determine timing and magnitude of exhumation of the region, we use Apatite (U-Th-Sm)/He thermochronometry (AHe).
215 This method makes use of the decay of radioactive isotopes and the temperature dependent retention of the daughter isotopes
($4He$) in apatite crystals (Zeitler et al., 1987; Wolf et al., 1996; Farley, 2000; Flowers, 2009). The low temperature sensitivity
(closure temperature) of 40 °C to 80°C (Zeitler et al., 1987; Wolf et al., 1996) makes AHe thermochronology a suitable
method to understand the cooling of the uppermost 2-3 km of the crust.

220 We collected samples from the siliciclastic Miocene Lower Freshwater Molasse (MOL), the Triassic Dinkelberg Formation ("Buntsandstein"; BST) and the Permian Weitenau Formation ("Rotliegend"; RL), as these lithologies are possibly apatite bearing (Lucas and Prevot-Lucas, 1997). In total, our samples span a vertical distance of 1370 meters. For the BST-RL section, we collected pieces of drill cores over intervals of roughly 25 meters for one sample, guided by internal stratigraphic boundaries (Fig. 2). We selected fine-grained sandstone sections of the core of about five to 30 centimeters in length. From

225 each interval we sample at least one meter of half cores. From the Molasse, only cuttings were available for sampling, which were washed and dried at 20 °C. We subdivided the Molasse based on stratigraphic boundaries, one sampling interval covering approximately 75 meters (Fig. 2).

We crushed all samples to release single grains and sieved the crushed material to obtain the 63 – 250 µm fraction. With this

230 fraction we performed heavy liquid separation with a sodium-polytungstate solution at 2.82 g/cm³. After investigation of the samples with a binocular, we re-separated the MOL samples with a solution of 3.0 g/cm³ density. The heavy fraction entered magnetic separation, using an Isodynamic Magnetic Separator (Model L-1, S. G. Frantz Co. Inc.). The red sandstone grains of the RL samples are covered by a thin coating of iron minerals. We removed the coating chemically using dithionite (after Tributh and Lagaly, 1986).

235

We selected apatites for dating from the final separates with a binocular. The preselected grains were further investigated with a transmitted light polarization microscope with magnifications of 5x to 50x. We checked for inclusions by immersing the grains in ethanol. Grain dimensions were measured by taking scaled images of the grains.

240 Apatite picking, as well as helium extraction and parent isotope measurements, have been carried out at the GÖochron Laboratories at the University of Göttingen (analytical procedure in von Eynatten et al., 2021). We measured 45 single grains from the Molasse section and 61 grains from the deeper BST and RL intervals (Table 1). We set up three classes according to the reliability of single grain ages. (1) Not reliable ages that are associated with high analytical errors (> 10 %, all values are smaller), low uranium concentration (< 10 ppm), substantial amount of helium measured on the first re-extract

245 (> 4 %) and improbably old ages that are most likely the result of parent isotope-rich insoluble inclusions (white, Table 1, Fig. 3). (2) Questionable ages of grains with analytical errors > 7.5 %, uranium concentrations < 15 ppm and first helium re-extracts >3 % (grey, Table 1, Fig. 3). (3) Reliable ages of all grains above these thresholds.
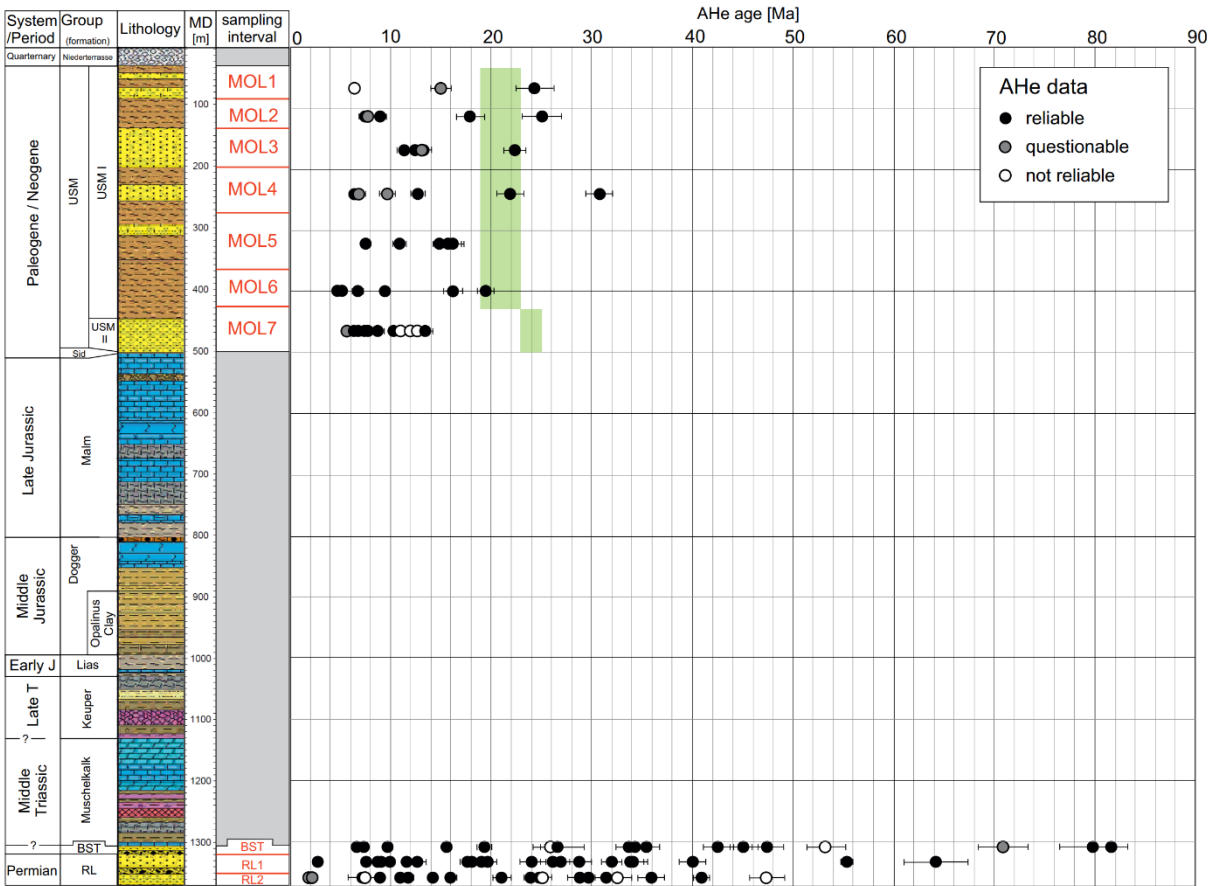
Figure 3. Measured AHe data plotted against sampling depth. Sampling intervals and depth ranges are indicated and named
250 **MOL1 – MOL7, BST, RL1 and RL2. Light green planes indicate stratigraphic ages. Stratigraphic age range of BST is 249 Ma to 244 Ma and 270 Ma to 260 Ma for RL (Kämpfen, 1972). Colors of data points indicate grains with analytical errors >10%, eU <10 ppm, first He re-extracts >4% or unrealistically high AHe ages (white, not reliable), analytical errors >7.5%, eU <15 ppm, first He re-extracts >3% (grey, questionable), others are called "reliable" (black).**

sampling interval	depth [m]	grain	raw age [Ma]	F_T	corrected age [Ma]	error [Ma]	analytical error [%]	U [ppm]	Th [ppm]	Sm [ppm]	He [ncc]	eU [ppm]	Th/U	sphere radius [µm]
MOL1	68	Mol-1 a1	12.2	0.50	24.4	1.9	4.4	30	4	233	0.0	31	0.14	36
		Mol-1 a2	4.4	0.69	6.4	0.4	3.4	9	42	381	0.0	18	4.83	54
		Mol-1 a3	9.5	0.63	15.0	1.0	4.2	14	25	213	0.0	20	1.79	44
MOL2	115	Mol-2 a1	12.8	0.51	25.0	1.9	3.3	48	59	112	0.1	62	1.24	35
		Mol-2 a2	5.0	0.66	7.7	0.5	3.9	27	40	196	0.0	36	1.49	49
		Mol-2 a3	4.3	0.55	7.8	0.9	9.4	14	39	329	0.0	23	2.75	41
		Mol-2 a4	9.3	0.52	17.9	1.3	3.0	30	91	378	0.1	52	2.97	36
		Mol-2 a5	5.6	0.62	9.0	0.5	3.2	24	45	229	0.0	35	1.87	48
MOL3	171	Mol-3 a1	16.2	0.72	22.4	1.1	2.4	53	67	413	0.4	69	1.25	56
		Mol-3 a2	8.8	0.77	11.4	0.7	5.4	15	32	239	0.0	23	2.15	62
		Mol-3 a3	8.7	0.70	12.5	0.6	2.7	32	45	169	0.1	43	1.38	55
		Mol-3 a4	7.7	0.59	13.2	0.9	2.9	32	119	622	0.1	60	3.75	42
		Mol-3 a5	11.0	0.83	13.2	0.8	5.3	15	21	246	0.0	20	1.43	79
MOL4	241	Mol-4 a1	4.2	0.66	6.4	0.4	2.8	24	78	497	0.0	42	3.23	46
		Mol-4 a2	5.5	0.56	9.8	0.7	5.1	15	31	238	0.0	22	2.13	39
		Mol-4 a3	7.7	0.61	12.7	0.7	2.1	70	82	364	0.1	90	1.17	45
		Mol-4 a4	3.8	0.55	6.9	0.6	5.3	10	23	216	0.0	16	2.32	40
		Mol-4 a5	22.1	0.72	30.9	1.3	1.9	57	19	238	0.8	61	0.34	60
		Mol-4 a6	14.8	0.67	22.0	1.3	2.8	141	13	203	0.4	144	0.10	46
MOL5	323	Mol-5 a1	7.2	0.66	10.9	0.6	3.2	47	57	408	0.1	60	1.23	46
		Mol-5 a2	4.3	0.57	7.6	0.5	2.7	62	42	388	0.1	72	0.69	40
		Mol-5 a3	10.1	0.62	16.2	1.0	3.4	24	15	107	0.1	28	0.60	44
		Mol-5 a4	10.3	0.69	15.0	0.7	2.8	96	23	382	0.1	101	0.24	52
		Mol-5 a5	8.9	0.56	15.8	1.3	4.2	22	67	386	0.0	38	3.03	35
MOL6	400	Mol-6 a1	4.6	0.66	6.9	0.5	5.5	20	90	588	0.0	41	4.45	51
		Mol-6 a2	15.0	0.77	19.5	0.8	2.3	62	14	383	0.5	65	0.22	69
		Mol-6 a3	7.3	0.76	9.5	0.3	2.1	92	45	405	0.1	102	0.49	59
		Mol-6 a4	10.0	0.61	16.3	0.9	2.2	49	3	308	0.1	50	0.05	45
		Mol-6 a5	2.3	0.47	4.8	0.4	5.6	13	78	134	0.0	31	6.15	34
		Mol-6 a6	3.0	0.57	5.3	0.4	4.5	55	50	153	0.0	67	0.90	36
MOL7	466	Mol-7 a1	6.7	0.61	11.1	0.9	6.1	9	11	303	0.0	12	1.18	44
		Mol-7 a2	5.3	0.59	7.9	0.5	4.3	23	40	263	0.0	32	1.72	49
		Mol-7 a3	4.8	0.54	8.7	0.7	4.6	34	10	186	0.0	37	0.30	34
		Mol-7 a4	3.4	0.53	5.8	0.5	5.6	15	10	97	0.0	17	0.64	41
		Mol-7 a5	5.9	0.69	8.8	0.5	3.1	25	41	322	0.0	35	1.63	49
		Mol-7 a6	7.0	0.65	10.4	0.6	2.7	83	36	378	0.1	91	0.43	49
		Mol-7 a7	9.8	0.56	12.0	0.5	2.7	52	10	303	0.2	54	0.20	79
		Mol-7 a8	8.2	0.67	12.8	0.8	2.8	56	15	233	0.1	59	0.26	48
		Mol-7 a9	8.9	0.55	13.5	0.7	2.6	75	19	352	0.1	80	0.25	49
		Mol-7 a10	4.5	0.58	7.6	0.5	2.3	187	100	248	0.1	211	0.53	39
		Mol-7 a11	3.5	0.67	6.5	0.5	5.2	40	19	177	0.0	45	0.46	36
		Mol-7 a12	3.6	0.67	6.8	0.5	3.6	70	34	278	0.0	78	0.49	41
		Mol-7 a13	4.8	0.82	7.0	0.3	2.8	66	26	353	0.1	72	0.40	58
		Mol-7 a14	4.2	0.64	6.5	0.4	3.6	20	10	240	0.0	22	0.51	48
		Mol-7 a15	7.6	0.66	13.4	0.8	2.4	51	38	267	0.1	60	0.75	44

Table 1. Analytical results of apatite (U-Th-Sm)/He dating from samples of the Bülach well, separated in the Molasse section (above) and BST-RL section (below). Depth is MD in the well, FT is alpha particle ejection correction, adjusted for grain geometry, sphere radius is the radius of a theoretical sphere resembling the grain volume. Colors refer to grains with analytical errors >10%, eU <10 ppm, first He re-extracts >4% or unrealistically high AHe ages (red, out of threshold), analytical errors >7.5%, eU <15 ppm, first He re-extracts >3% (questionable, orange).

sampling interval	depth [m]	grain	raw age [Ma]	F_T	corrected age [Ma]	error [Ma]	analytical error [%]	U [ppm]	Th [ppm]	Sm [ppm]	He [ncc]	eU [ppm]	Th/U	sphere radius [µm]
BST	1318	BST3 a1	39.5	0.87	45.2	1.4	2.5	87	11	304	15.6	90	0.12	119
		BST3 a2	13.8	0.88	15.6	0.5	2.4	68	18	269	1.3	73	0.27	130
		BST3 a3	66.8	0.84	79.9	3.4	3.5	122	15	287	18.4	125	0.12	91
		BST3 a4	40.8	0.86	47.5	1.6	2.5	172	14	193	13.5	175	0.08	107
		BST-3 a6	71.8	0.88	81.7	2.5	2.5	91	15	275	18.5	95	0.16	124
		BST-6 a1	34.5	0.81	42.6	1.5	2.2	55	20	267	2.1	59	0.37	79
		BST-6 a2	5.6	0.75	7.5	0.3	2.3	41	19	231	0.1	46	0.47	63
		BST-6 a3	7.2	0.74	9.8	0.4	2.2	35	58	302	0.2	49	1.64	60
		BST-6 a4	4.7	0.69	6.7	0.3	2.4	36	23	311	0.1	42	0.64	57
		BST-6 a5	14.9	0.77	19.3	0.7	1.9	132	17	269	1.4	136	0.13	67
		BST-6 a6	27.3	0.77	35.4	1.3	1.9	85	17	235	1.7	89	0.21	71
		BST-8 a1	21.8	0.82	26.7	1.0	2.5	65	20	282	1.6	69	0.30	82
		BST-8 a2	20.6	0.79	25.9	1.0	2.5	64	18	296	1.0	68	0.28	73
		BST-8 a4	42.2	0.79	53.3	1.9	2.4	36	21	235	2.4	41	0.58	83
		BST-8 a5	29.0	0.84	34.4	1.1	2.4	40	19	252	2.6	45	0.48	97
		BST-8 a6	59.1	0.83	70.9	2.5	2.4	51	21	346	4.9	55	0.41	91
		BST-8 a7	25.6	0.76	33.8	1.4	2.4	47	52	296	0.8	59	1.10	67
RL1	1335	RL1-6 a1	23.7	0.70	33.9	1.6	2.5	99	24	274	0.9	104	0.25	54
		RL1-6 a2	10.0	0.79	12.7	0.5	2.5	101	25	338	0.6	107	0.24	70
		RL1-6 a3	12.0	0.68	17.8	0.9	2.5	129	13	275	0.5	133	0.10	53
		RL1-6 a4	17.9	0.74	24.1	1.1	2.6	108	12	326	0.5	111	0.11	57
		RL1-6 a5	42.4	0.66	64.2	3.2	2.5	51	33	264	0.7	58	0.65	53
		RL1-6 a6	15.4	0.78	19.8	0.8	2.5	150	13	217	1.6	153	0.08	74
		RL1-6 a7	2.0	0.71	2.9	0.2	3.7	35	23	387	0.0	40	0.67	57
		RL1-6 a8	18.5	0.71	26.2	1.3	2.6	77	16	230	0.4	81	0.21	54
		RL1-6 a9	310.4	0.71	438.4	37.5	7.6	133	35	206	0.9	141	0.27	58
		RL1-6 a10	20.2	0.75	27.0	1.2	2.5	136	25	220	1.0	142	0.18	59
		RL1-6 a11	42.3	0.76	55.4	2.4	2.6	57	14	229	1.1	60	0.25	63
		RL1-6 a12	13.1	0.72	18.2	0.9	2.6	129	17	300	0.4	133	0.13	54
		RL1-6 a13	23.7	0.74	32.1	1.5	2.5	294	22	282	1.9	299	0.08	57
		RL1-6 a14	6.8	0.78	8.7	0.4	2.4	62	22	386	0.2	67	0.36	68
		RL1-9 a1	27.4	0.80	34.1	1.1	1.9	141	12	247	4.7	143	0.08	86
		RL1-9 a2	6.8	0.75	9.1	0.4	2.0	62	15	295	0.3	66	0.24	66
		RL1-9 a3	32.3	0.81	40.0	1.3	1.9	234	19	263	6.5	238	0.08	83
		RL1-9 a4	14.5	0.76	19.1	0.7	1.9	106	27	291	0.7	113	0.25	66
		RL1-9 a5	5.3	0.69	7.7	0.4	2.2	29	78	108	0.1	48	2.67	55
		RL1-9 a6	7.4	0.75	10.0	0.4	2.0	70	23	260	0.2	75	0.33	61
		RL1-9 a7	22.1	0.77	28.9	1.1	1.9	161	16	361	2.1	164	0.10	72
		RL1-9 a8	9.1	0.78	11.7	0.2	1.9	197	25	270	0.9	203	0.13	70
RL2	1360	RL2-8 a1	5.5	0.74	7.5	0.3	2.9	9	17	147	0.1	13	1.89	65
		RL2-8 a2	5.9	0.80	7.3	0.3	2.5	36	26	356	0.2	42	0.74	76
		RL2-8 a3	13.3	0.83	16.0	0.5	2.4	70	28	307	1.8	76	0.41	96
		RL2-8 a4	22.0	0.76	28.9	1.3	2.5	144	28	235	1.6	150	0.20	62
		RL2-8 a5	21.4	0.72	29.8	1.4	2.4	157	52	264	1.6	169	0.33	58
		RL2-8 a6	8.8	0.75	11.8	0.5	2.5	66	25	241	0.4	72	0.38	66
		RL2-8 a7	24.9	0.76	32.6	1.3	2.4	66	26	249	1.6	72	0.39	69
		RL2-8 a8	33.7	0.82	40.9	1.5	2.5	84	20	263	4.0	89	0.23	85
		RL2-8 a9	38.5	0.81	47.4	1.8	2.4	55	33	270	2.7	63	0.60	81
		RL2-8 a11	6.6	0.74	9.0	0.4	2.5	76	28	298	0.4	82	0.37	64
		RL2-8 a12	8.6	0.78	11.0	0.5	2.5	94	28	310	0.4	100	0.30	70
		RL2-8 a14	1.5	0.71	2.1	0.2	5.9	13	25	190	0.0	19	1.90	54
		RL2-8 a16	20.8	0.82	25.2	0.8	2.2	99	44	198	3.5	109	0.45	101
		RL2-8 a17	28.5	0.79	35.9	1.4	2.3	250	46	293	4.0	261	0.18	72
		RL2-8 a18	11.0	0.78	14.3	0.5	2.2	129	47	298	1.1	140	0.37	76
		RL2-8 a19	23.6	0.82	28.9	1.0	2.2	135	54	324	3.0	148	0.40	84
		RL2-8 a21	20.1	0.84	24.0	0.8	2.2	113	38	349	3.8	122	0.33	100
		RL2-8 a22	18.9	0.76	25.0	1.1	2.2	165	44	258	1.2	175	0.27	62
		RL2-8 a23	15.0	0.71	21.1	0.9	2.3	180	36	267	1.2	188	0.20	63
		RL2-8 a24	1.8	0.79	2.3	0.1	3.7	13	34	293	0.0	21	2.57	75
		RL2-8 a25	25.3	0.80	31.5	1.2	2.2	96	37	312	1.9	105	0.38	77

260

3.2 Modeling

In order to constrain the thermal history, we apply different modeling approaches, with the ultimate goal to arrive at a consistent thermal history for the basin. In particular, we use HeFTy v.1.9.3 (Ketcham, 2005), QTQt 64R5.6.9.0 (Gallagher, 2012) and PyBasin (Luijendijk et al., 2011). HeFTy uses a 'frequentist' approach, where statistical tests evaluate the fit of
265   the thermal model to the data (Ketcham, 2005; Vermeesch and Tian, 2014). QTQt uses an inversion procedure based on Bayesian Markov Chain Monte Carlo algorithm to determine the best time-temperature path reproducing the AHe dataset (Gallagher, 2012; Vermeesch and Tian, 2014). Both tools have been extensively discussed and compared (Vermeesch and Tian, 2014, 2018; Gallagher and Ketcham, 2018). PyBasin uses a forward modeling approach, where burial and exhumation timing are defined as parameters instead of the program searching for possible t-T paths. PyBasin is the only one of the three
270   tools that allows to include different provenance histories into the model. In addition to inverse modeling, we take advantage of forward modeling in PyBasin in order to test specific burial, exhumation and heat flow scenarios. In addition to thermochronometric data, we include published vitrinite reflectance, stratigraphic, as well as paleo-temperature and heat flow data to constrain the burial history of the basin.

275   **4 Results**

4.1 AHe-data

Most of the AHe ages within the Molasse section (down to 500 m) are younger than their respective stratigraphic age (Fig. 3, Table 1). This indicates at least partial reset after deposition. The data exhibits an age spread from 4-5 Ma to roughly 30 Ma, which decreases systematically with depth to ages ranging between 5 and 14 Ma at a depth of 430 m to 500 m. This pattern
280   can be indicative for an exhumed partial retention zone (PRZ) (e.g., Fitzgerald et al., 2006). If an exhumed PRZ is responsible for the age-depth trend, extrapolation would imply complete reset for the Molasse section at a depth just below 600 m. The base of the partial retention zone is commonly estimated to indicate a paleo-temperature of around 70°C for the AHe system (Zeitler et al., 1987; Wolf et al., 1996, see above). Using the recent geothermal gradient of 35 °C/km (Nagra, 2020), this temperature is expected at a depth of around 1700 m. The difference of this depth and estimated base of the
285   exhumed PRZ translates into a first rough exhumation estimate of 1100 m.

AHe ages of the BST-RL interval (1306 m – 1370 m) are all much younger than their respective stratigraphic ages (Fig. 3). They exhibit a spread from roughly 3 Ma to 82 Ma at the top BST. Comparable to the Molasse section, the age spread decreases towards the bottom of the section. Maximum ages for the RL1 interval are 64 Ma and for the RL2 interval the
290   oldest grain measured has an AHe age of 41 Ma.

Comparing both sampled sections (the upper Molasse section and the lower BST-RL section), the large age spread in the lower section is surprising, as based on results in the Molasse data, a complete reset of ages would be expected below 600 m. and definitely above 1300 m. Two different explanations for this observation can be put forward. Either the BST-RL and the MOL sample sets share the same PRZ. This would imply that the observed age spread is the result of grain properties such as eU or grainsize (e.g., Farley, 2000; Fillon et al., 2013). Alternatively, the two sample sets have a different PRZ, i.e. they are sensitive to different temperature intervals and consequently represent different thermochronometers. This may be the consequence of different provenance histories (Luijendijk et al., 2011). To probe into this, we examine the available data on element concentrations and grainsize for correlations with the AHe age.

4.2 Correlations of AHe ages with grain size and chemistry

A weak positive correlation between grain size and age can be observed (Fig. 4a). Logarithmic fits give best R^2 values. For the whole dataset we calculate an R^2 value of 0.04. This correlation is stronger for the BST grains ($R^2 = 0.32$), while barely visible for Molasse grains ($R^2 = 0.11$). RL grains even show a negative correlation with lower AHe ages for larger grains ($R^2 = 0.02$). We note that even though larger than standard AHe datasets, correlation coefficients are still sensitive to single datapoints. Especially the stronger correlation obtained for the BST subset depends largely on the ages of the two largest grains. We observe that Molasse grains are relatively small compared to BST-RL grains and we also measured younger ages for the Molasse grains. However, a relatively small Molasse grain can have a relatively old AHe age, while a relatively large BST-RL grain can have a young AHe age. Consequently, grain size alone cannot explain the observed age pattern, and if at all, then only in few cases.

The plot of AHe ages versus eU (Fig. 4b) similarly shows only weak correlation trends ($R^2 = 0.06$ for the entire dataset). Any specific eU value is associated with a wide range of AHe ages. The majority of Molasse grains shows eU values ranging from 0 ppm to 100 ppm and respective AHe ages ranging between 4 Ma and 20 Ma ($R^2 = 0.05$). It can be observed that Molasse grains with eU values lower than 25 ppm show AHe ages below 16 Ma, while AHe ages for grains with eU concentrations of 25 ppm to 80 ppm exhibit the full observed range from 4 Ma to 30 Ma. However, this difference is marked by only a few grains. Similarly, for BST grains a correlation between eU and apparent age cannot be established for the entire data set ($R^2 = 0.09$). It can only be observed that RL grains of eU values below 50 ppm have AHe ages below 10 Ma. For eU values above of 50 ppm, the correlation is much weaker with the oldest grains exhibiting eU values around 60 ppm. Grains of higher eU show no correlation with ages spreading from around 10 Ma to 40 Ma ($R^2 = 0.03$).

AHe age vs. Th/U reveals that BST-RL grains typically show Th/U ratios below 1.0, while AHe ages spread from 2 to 82 Ma (Fig. 4c). Molasse grains spread along the Th/U axis with values up to over 6.0, whereas the age spread is narrow with a maximum value of 30 Ma. Furthermore, the Th/U ratio of the Molasse samples collected from different stratigraphical levels

325 allows identifying a characteristic change in the source lithologies during Miocene. The younger sediments (samples MOL1 to MOL4) contain a higher proportion of apatite crystals with Th/U ratio above one than the older layers (samples MOL5 to MOL7, Fig. 4d). This change can be associated with the exhumation of different basement formations in the catchment area within the Central Alps, indicating a change (presumably younging) of the primary cooling ages (e.g., Spiegel et al., 2001).

330
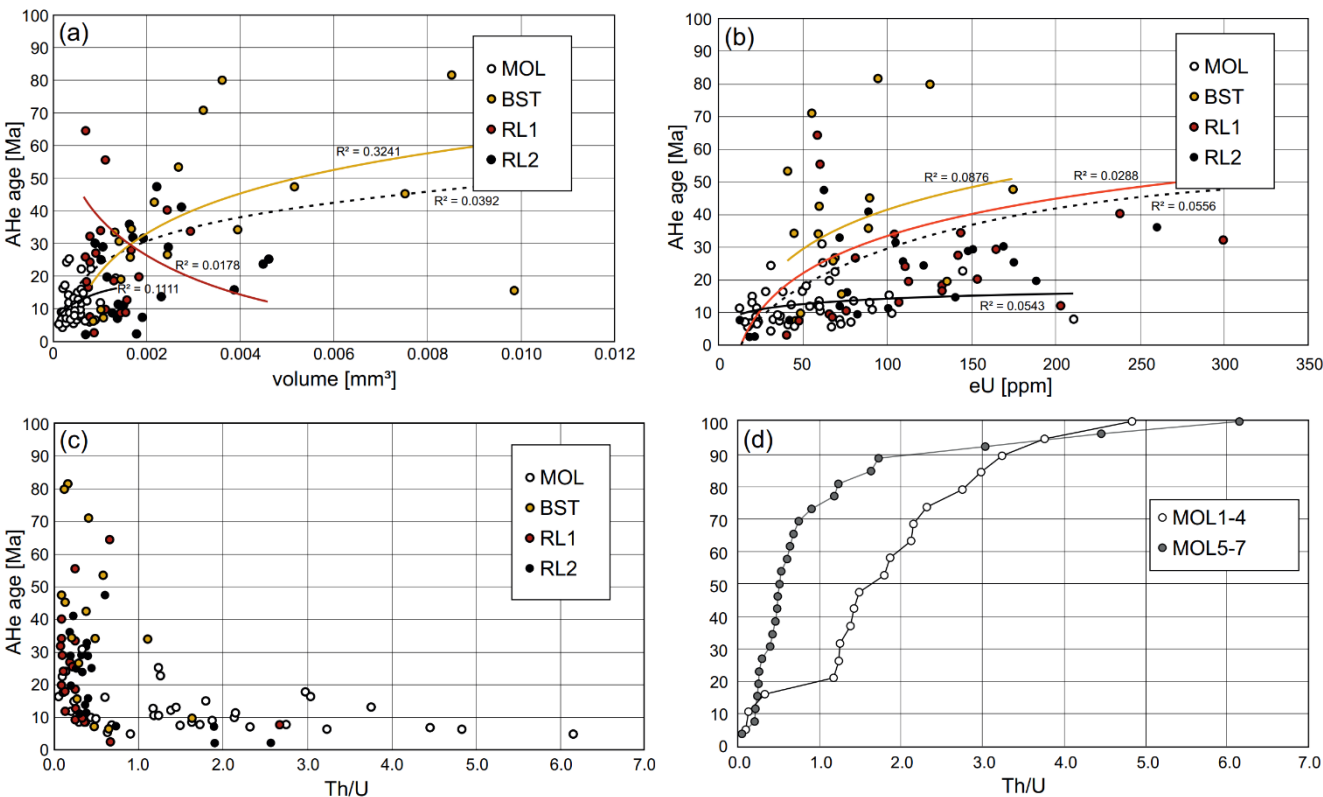
Figure 4. AHe age vs. grain properties, with logarithmic fits and R² values for volume and eU, where RL1 and RL2 are computed together. Line-color correspond to the sampling interval, dashed black line for all data. a) AHe age vs. grain volume. b) AHe age vs. effective uranium concentration (eU). c) AHe age vs. thorium over uranium ratio. d) Molasse thorium over uranium ratios separated into intervals MOL1-4 and MOL5-7.

335

In sum we observe a weak correlation of grainsize and eU with AHe age, while no correlation between Th/U and AHe age is apparent. We note however, that BST-RL grains have low Th/U ratios, while Molasse grains exhibit Th/U values ranging between 0 and 6 (Fig. 4c, Table 1). Additionally, Th/U ratios of the Molasse grains allow for a separation of the sample set into two provenance-related subsets (Fig. 4d).

340

4.3 Thermal modeling with HeFTy

We define a set of boundary conditions for each model computed with HeFTy (Ketcham, 2005). These are the regional thermal parameters surface temperature and basal heat flow. For all parameters, only constants can be set in HeFTy. We choose 12 °C as mean value of the annual surface temperature for the region from Miocene to recent times (Mosbrugger et

345   al., 2005), including glaciation phases. We set a mean value for heat flow of 80 mW/m² over the relevant time span from at least Molasse deposition to recent values (e.g., Mazurek et al., 2006; Omodeo-Salé et al., 2021). With HeFTy, we model all samples separately (MOL1 - MOL7). For each, we create one model using the grains with youngest AHe ages and one of the oldest AHe ages. Modeling of all grains of a sample or even multi-sample models fail to find paths of acceptable fits. We combine forward and inverse modeling by predefining an exhumation path with a good fit and subsequently run inverse

350   models. For these, we constrain the deposition time as the range of stratigraphic ages (e.g., Kempf et al., 1997; Schlunegger et al. 1997) and allow a temperature range at the time of deposition of 15 °C +/- 5 °C. This range accounts for the paleo-temperatures of about 15 °C obtained by Mosbrugger et al. (2005) and considers uncertainties over the time span. We assume a maximum temperature after deposition for Molasse grains of 90°C, as the grains have only been partially reset. We did not limit rates of temperature changes. The present temperature of each sample is constrained by measured borehole

355   temperatures (Nagra, 2020). We set the number of paths tried to 10.000 for each model. We use the HeFTy standard goodness of fit (GOF) merit values for good and acceptable paths that are 0.5 and 0.05, respectively (Ketcham, 2005). As helium diffusion models, we use the algorithm of Farley (2000) and Flowers (2009). Results of both diffusion models are similar for the Molasse samples, even though the algorithm of Farley (2000) produces more good and acceptable paths than obtained with the RDAAM model (Flowers, 2009).

360

We show the results of these models in Figure 5. All models indicate heating and subsequent cooling after deposition, while exhibiting a wide range of pre-depositional paths. This is an expected result, given the (partial) reset of the samples in the basin. The average paths of the models differ with respect to timing and magnitude of heating and cooling. Onset of cooling for the young Molasse grains varies from 10 to 16 Ma with maximum temperatures from 74°C to 84 °C. Many of the single

365   paths suggest rapid cooling at around 6 Ma. However, we note that this is not the only viable solution, and t-T histories with more continuous cooling provide similarly good fits. This is also witnessed in the weighted average paths, which all indicate cooling rates in the range of 3.5 °C/Ma to 6 °C/Ma.

We note that the young and old grains of a single interval often suggest different timing for maximum temperature. Models

370   including only the oldest grains of the Molasse samples, maximum temperatures were reached between 12 and 17 Ma (Fig. 5). Peak temperatures of the average models vary from below 40 °C to 85 °C. As for the young grains, modeled peak temperatures are not strictly ordered by depth of the sample, even though there is a trend to higher peak temperatures for deeper samples (Fig. 5). Cooling rates obtained by the weighted average paths range from 1.5 °C/Ma to 3.5 °C/Ma.

375
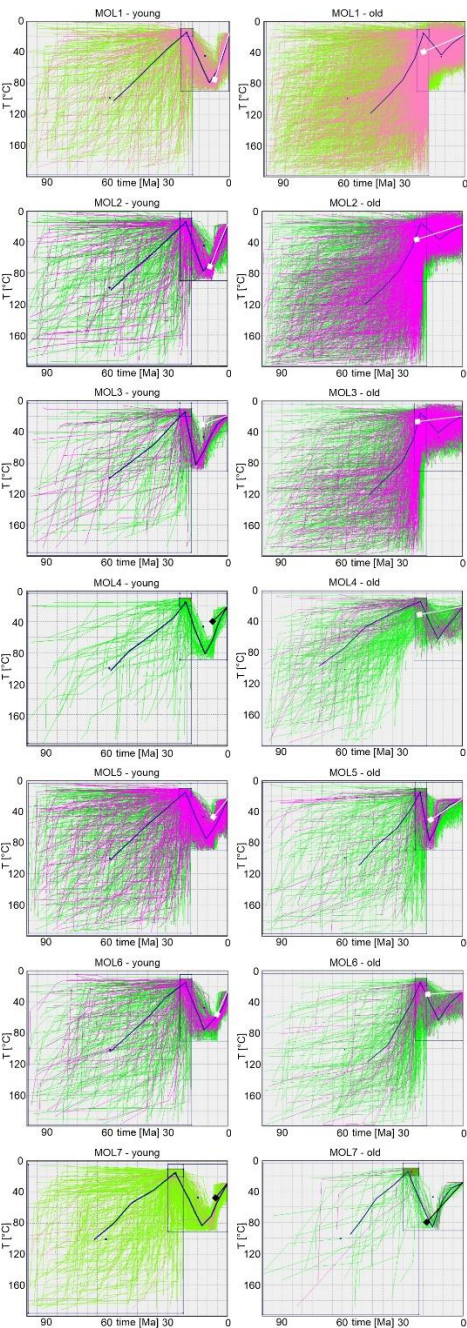
Figure 5. t-T models of the Molasse grains obtained using HeFTy software (Ketcham, 2005) 10.000 iterations were run. Diffusion model is Farley (2000); models with RDAAM (Flowers et al., 2009) give similar results. Left: youngest group of grains per sample (MOL1 – MOL7), right: oldest group of grains. Square with line (black or white depending on best visibility) mark the forward constraint producing best fits for the grain(s) modelled. Boxes are constraints for inverse modeling: pre-depositional, t-T range of deposition and re-heating and cooling after deposition. Pink paths resemble "good" models (GOF merit value >0.5), green paths "acceptable" models (GOF merit value >0.05, Ketcham, 2005).

380

HeFTy models of the BST-RL grains are shown in Figure 6. We present seven models, separating single grain ages by depth and age: young, medium and old grains of the Buntsandstein interval (Fig. 6a, 6b, 6c), medium-young grains of interval RL1

385 (Fig. 6d, 6e), and medium-old grains interval RL2 (Fig. 6f, 6g). All models are constrained based on previous work on basin evolution, as well as the fact that our samples have only seen partial reset (see above). We constrain maximum burial from 60 to 80 Ma with a temperature window of 40 to 90°C. To account for Cretaceous-Paleogene exhumation, we allow for cooling to 20 to 60°C between 37.5 and 60 Ma. Molasse sedimentation started after a phase of hiatus, which is why we constrain another box of the same temperature range from 25 to 37.5 Ma. Apart from the recent temperature of the respective

390 samples, we define a constraint of 60 to 120°C from 0 to 18 Ma to account for maximum burial in the Molasse stage. We tested the diffusion model of Farley (2000) and RDAAM (Flowers, 2009). HeFTy produces acceptable and few good paths only for few or single grains using RDAAM, even though we decreased the GOF merit values to 0.01 and 0.1, respectively.

The weighted mean paths of the seven modeled subsets all show rising temperatures until Cretaceous times and subsequent

395 cooling before Molasse burial. Single paths avoid Cretaceous/Paleogene cooling. Pre-Molasse maximum temperatures have been reached at the end of the Cretaceous, between 67 and 72 Ma. The temperatures modeled at these times range from 70 °C to just above 90 °C. Note that the youngest samples modeled do not necessarily give the hottest maximum temperatures, nor is the time spent at high temperatures longer. Cooling paths of the seven models differ with respect to their Molasse-stage re-heating. Timing of the lowest temperature obtained ranges between 30 Ma and 57 Ma. Temperatures reached during

400 this time range from just above 20 °C to 40 °C. Models of younger samples indicate grains have spent shorter times at low temperatures with slower cooling and more rapid re-heating. They do however not show higher minimum temperatures.

Re-heating within the Molasse stage reaches maximum temperatures of 80 °C to 110 °C in the time interval from 2 to 12 Ma. The old BST subset marks an outlier with a maximum temperature of 80 °C at 2 Ma (Fig. 6c). Note that this mean path is

405 based on only three acceptable paths, even with the reduced GOF merit value. The range of maximum temperatures is shifted by about 30 °C to higher values compared to the Molasse sample set, which resembles the vertical distance. However, single models are in conflict with the Molasse models, as their expected maximum temperatures and heating/cooling rates are too low to account for the vertical distance.

410 In summary, HeFTy models of the Molasse sequences produce good results when modeling single grains or few grains of comparable AHe ages of the same sample. Nonetheless, the single models cannot be reconciled into a consistent thermal history. For the Molasse, onset of cooling ranges between 10 and 17 Ma. Peak temperatures show a wide range of possibilities, with values from 40 °C and 85 °C, which is a much larger span than expected for 500 m of depth interval. Furthermore, modeled peak temperatures are not consistently increasing with depth. The models consequently imply a range

415 of different cooling rates from 1.5 °C/Ma to 6 °C/Ma. BST-RL samples can barely be modeled using HeFTy. Only using

RDAAM as diffusion model and decreasing the GOF merit values yields a limited amount of possible t-T histories. These paths are difficult to reconcile with models of the Molasse samples.
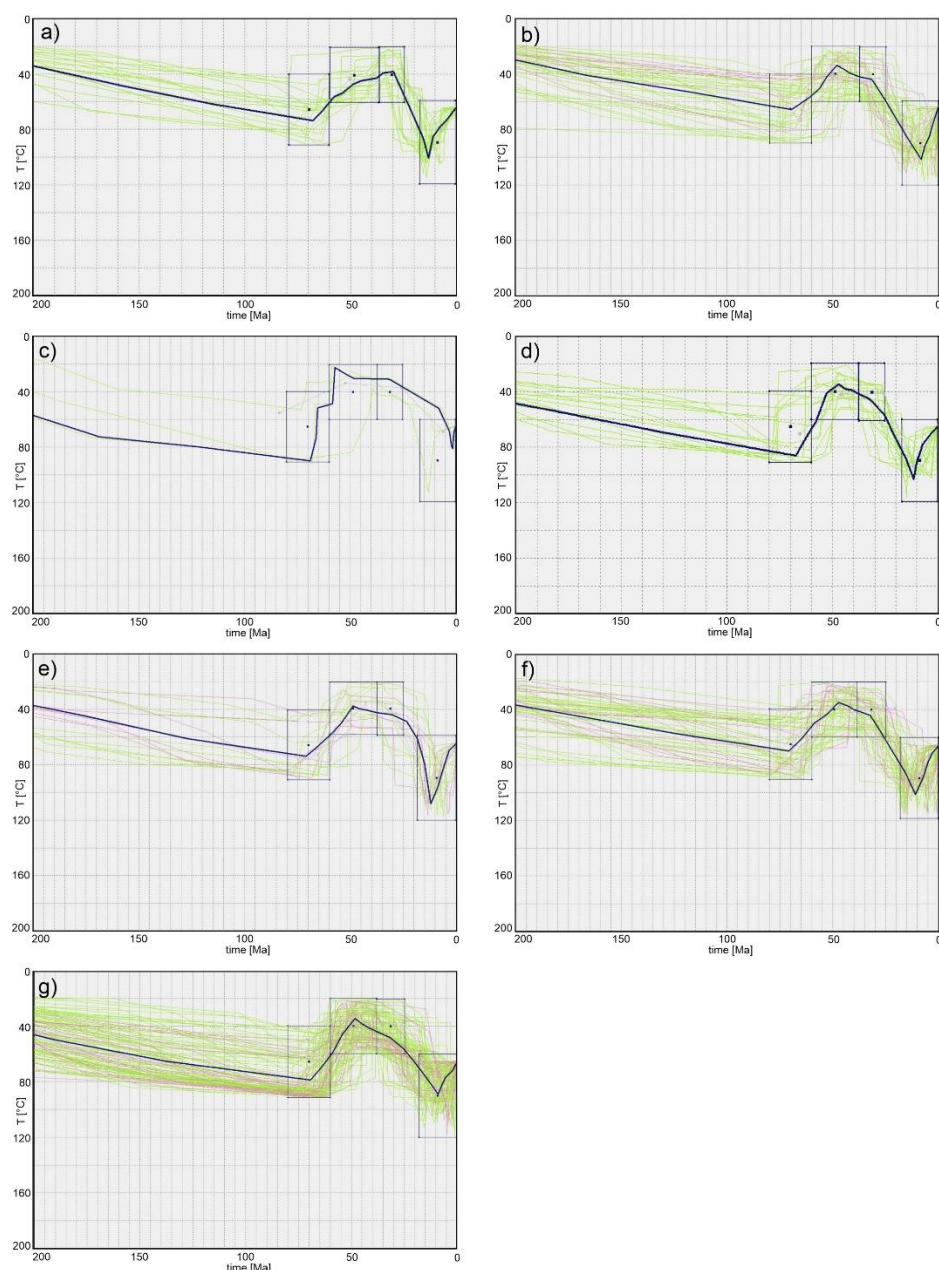
420 **Figure 6. t-T models of the Molasse grains obtained using HeFTy software (Ketcham, 2005) 10.000 iterations were run. Diffusion model is RDAAM (Flowers et al., 2009). a) BST_A: AHe age 6 to 10 Ma, b) BST_B: AHe age 45 Ma, c) BST_C: AHe age: 78 to 81, d) RL1_A: AHe age: 16 to 19 Ma, e) RL1_B: AHe age: 31 Ma, f) RL2_A: AHe age: 7 Ma, g) RL2_B: AHe age: 47 Ma. Pink paths resemble "good" models (GOF merit value >0.1; Ketcham, 2005), green paths "acceptable" models (GOF merit value >0.01). Dark blue path is the weighted average path.**

4.4 Thermal modeling with QTQt

QTQt is well-suited to model vertical profiles because it allows for simultaneous models of multiple samples with known vertical separation (Gallagher, 2012). This approach is different from modeling with HeFTy, where we modeled single sub-samples and few grains separately. The QTQt models presented in this study are based on a stable solution obtained after 10.000 model iterations; the final model is provided as the expected model (weighted mean model). We constrain the recent borehole temperature profile (Nagra, 2020), as well as the surface temperature at the time of deposition of the individual strata (green box for Molasse in Fig. 7; Mosbrugger et al., 2005). Further time-temperature constraints implemented are based on previous studies and geological evidence, such as maximum burial before exhumation in Paleogene times (e.g., Mazurek et al., 2006; Strasser et al., 2016; Omodeo-Salé et al., 2021). We allow a broad range of 70 °C +/- 30 °C from 65 to 45 Ma (Fig. 7). Following this cooling event, we constrain temperatures of 25 °C +/- 15 °C for the time span of 30 to 40 Ma. This temperature window resembles a maximum depth of 850 meters, given that the BST-RL section is only overlain by the drilled Jurassic successions at this time (Fig. 2). The youngest constraint is based on our observed Miocene AHe cooling ages. Prior to Miocene cooling, we constrain maximum temperatures of 70 °C +/- 30 °C from 13 to 5 Ma. As for HeFTy, we test two diffusion models (Farley, 2000; Flowers, 2009), which result in similar model outputs.

The resulting thermal history model for the BST-RL samples (hottest sample; red line in Figure 7a) shows maximum temperatures of just below 120 °C at 60 Ma, with broad 95% credible intervals of +/- 60 °C (pink paths). After 30 Ma a cooling phase ends with temperatures of just below 50 °C with 95% credible intervals of +/- 30 °C. Reheating after Molasse deposition results in 60 °C with 95% credible intervals of +/- 30°C for the top-most Molasse sample (coldest sample; dark blue line) and 110 °C with 95% credible intervals of +/- 50 °C for the BST-RL samples.

Towards present day temperatures, the 95% credible intervals of the coldest sample (Molasse) and hottest sample (BST-RL) do not show a similar behavior, increasing the temperature offset exponentially around 12 Ma. As the deviation of thermal histories occurs from maximum burial to recent temperatures, we allow a model run without constraining the recent temperature profile. The result is a single consistent thermal history, as the uncertainty ranges show consistent cooling paths (Fig. 7b). The declining distance between the temperature paths of the single samples shows that a very low recent geothermal gradient of 5 °C/km would be needed to arrive at this model.

In addition to computing the best paths, QTQt generates probabilistic figures for the temperature history for each sample modeled (Fig. 8). These show that for the Molasse section, probabilities are highest around the best paths shown in Figure 7a. Whereas BST-RL probabilities are comparably low over the whole area of computed paths. This indicates that over all iterations of modeling, each path within this broad range was equally likely to be obtained. To solve these inconsistencies, a

tool that takes heat flow changes over time and provenance age as input data is required, thereby allowing to model the Molasse and BST-RL sample sets together.
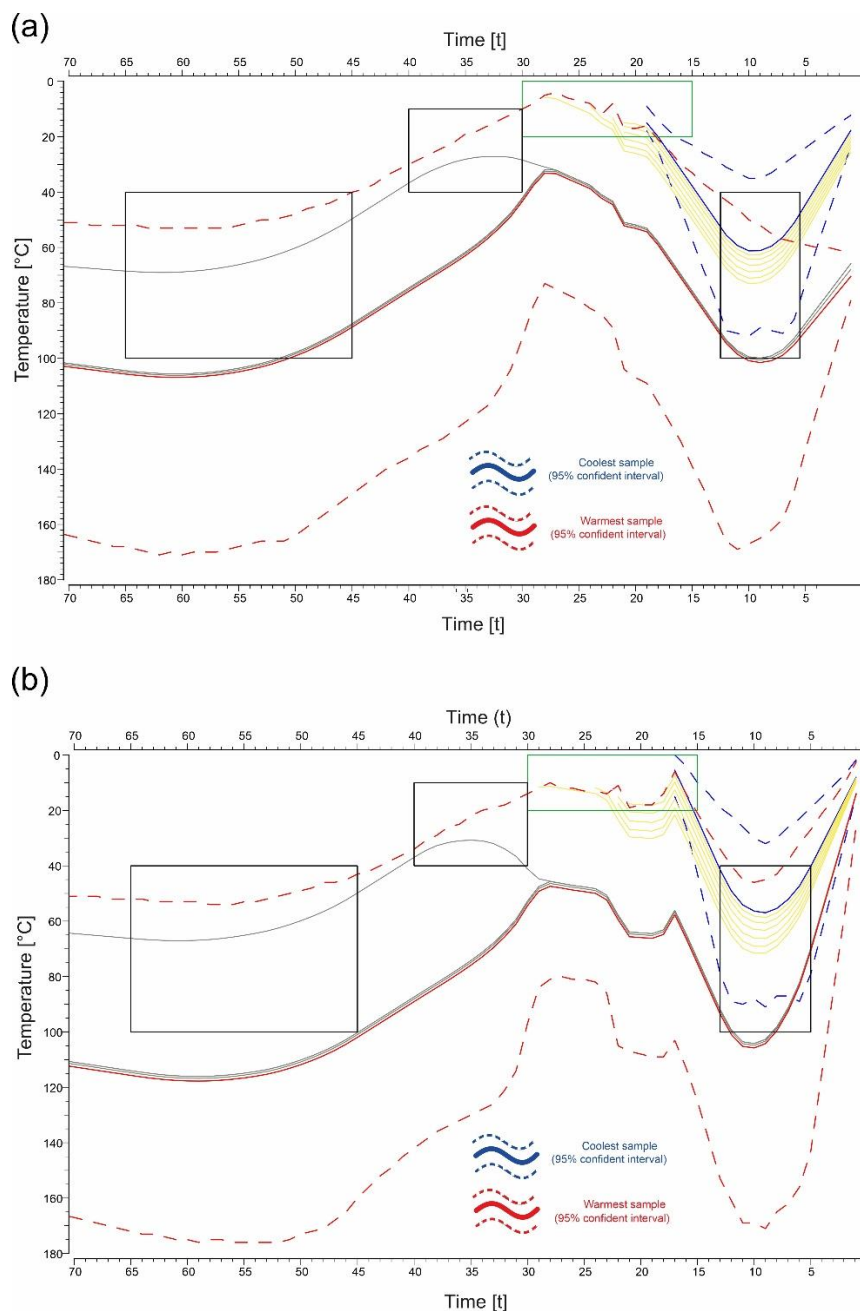
Figure 7. Modeling results using QTQt (Gallagher, 2012). Black boxes are t-T constraints for inverse modeling, green box is the t-T constraint for the deposition of Molasse sediments. The models are the stable solutions after 10.000 iterations. Red line is the resulting t-T path for the deepest sample (RL2), with pink lines marking the 95% credible intervals. Dark blue line is the resulting t-T path for the shallowest sample (MOL1), with light blue lines showing the 95% credible intervals. a) Model with measured borehole temperatures as constraints, b) without constrained recent temperatures.
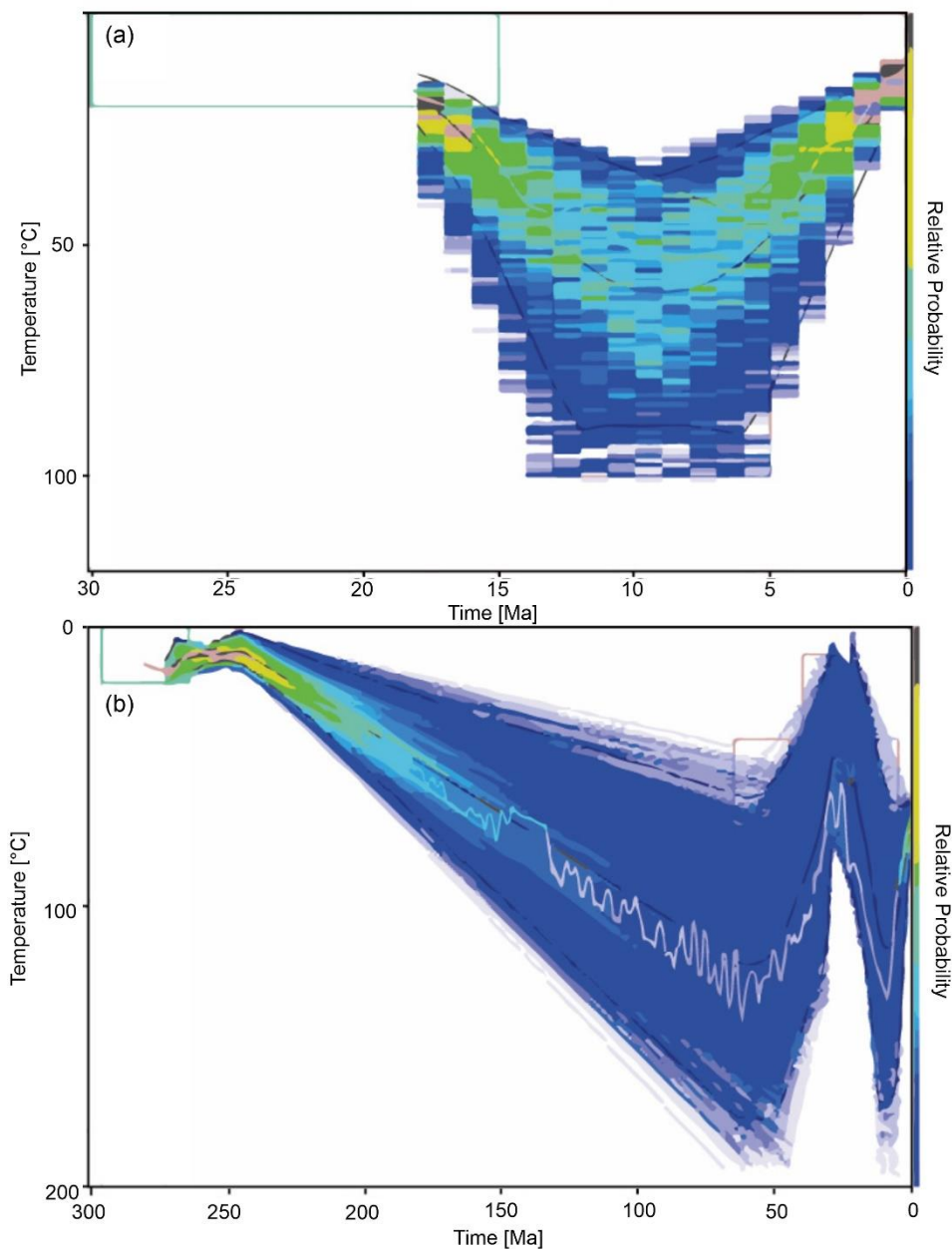
Figure 8. Probability fields from 10.000 model runs of QTQt, exemplarily shown for MOL1 (a) and RL2 (b). MOL2-7 shows similar results with lower maximum probabilities at depth. BST and RL1 are similar to RL2. Rose implies high probability of the model runs obtaining the t-T path through the respective field; blue colors indicate low probability.

465

4.5 Thermal modeling with PyBasin

4.5.1 Best fit model including all samples

In PyBasin (Luijendijk et al., 2011) a stratigraphic column can be implemented, and rock properties can be assigned for each lithology (Tables 2, 3). We compile the lithologic composition of each unit using mineralogic data from measurements on cuttings and drill cores (Nagra, 2020). Measurements for rock density, surface porosity and compressibility exist as well. Thermal conductivity and heat capacity have been measured on drill cores of the Weiach well (location in Fig.1, Mazurek et al., 2006). As diffusion model, we use the algorithm of Farley (2000).

stratigraphic unit	strat. ages [Ma]		lithologic components [%]										provenance histories [Ma]							
	bottom	top	congl.	sand	silt	clay	limst.	dolo.	marl	anhy.	hal.	coal	start 1	end 1	start 2	end 2	start 3	end 3	start 4	end 4
OSM	17.25	13	0.100	0.300	0.300	0.100	0.200						22	16	24	20	22	16	24	20
OMM	19	17.25	0.100	0.720	0.050	0.050	0.080						23	19	24	21	23	19	24	21
USM_II_top	20	19		0.350	0.200				0.450				23	20	25	22	23	20	25	22
USM_II_tm	21	20		0.350	0.200				0.450				24	21	25	22	24	21	25	22
USM_II_mb	22	21		0.350	0.200				0.450				25	22	26	23	25	22	26	23
USM_II_base	23	22		0.350	0.200				0.450				26	22	27	23	26	22	27	23
USM_I	25	23		0.600	0.250				0.150				28	23	29	26	28	23	29	26
Siderolithikum	42	31				0.100	0.900						150	50	110	50	80	50	150	140
Cretaceous	145	65					1.000						247	153	218	153	198	153	247	237
Fels_Masse	149	145				0.025	0.950		0.025				249	157	221	157	200	157	249	239
Schwarzbach_FM	151	149			0.075		0.675		0.250				250	158	223	158	201	158	250	240
Villigen_FM	153	151					0.850		0.150				251	160	225	160	202	160	251	241
Wildegg_FM	155	153		0.050	0.050		0.300		0.600				252	162	227	162	203	162	252	242
Dogger_top	168	165			0.200	0.250			0.550				262	176	236	176	211	176	262	252
Herrenwis	170	168			0.050		0.850		0.100				264	176	238	176	212	176	264	254
Dogger_Clay	180	170			0.125	0.175	0.475		0.125				270	186	245	186	220	186	270	260
Staffelegg_FM	200	180			0.250	0.050	0.300		0.400				286	205	257	205	235	205	286	276
Klettgau_FM	225	200		0.150	0.100			0.350	0.400				306	229	282	229	255	229	306	296
Baenkerjoch_FM	233	225				0.100	0.250		0.150	0.500			311	236	287	236	261	236	311	301
Schinznach_FM	240	233			0.050	0.050	0.300	0.600					316	242	292	242	266	242	316	306
Zeglingen_FM	242	240				0.150			0.200	0.400	0.250		317	244	294	244	267	244	317	307
Kaiseraugst_FM	244	242		0.125	0.125	0.175	0.050	0.125		0.400			318	245	296	245	268	245	318	308
Dinkelberg_FM	249	244	0.450	0.350	0.100	0.050			0.050				320	250	300	250	270	250	320	310
Weitenau_FM	270	260	0.150	0.650	0.050	0.150							320	265	300	265	270	265	320	310

Table 2. Stratigraphic column with stratigraphic ages, lithologic components and provenance histories. Stratigraphic age ranges were taken from Kämpfen (1972), lithologic composition from Nagra (2020), provenance histories based on tectonic models of the Alps by Egli et al. (2017a), Glotzbach et al., (2011b), Herwegh et al., (2017, 2020), Hurford (1986), Kissling and Schlunegger (2018), Schmid et al. (2004). Start is the time at which cooling below 120°C occurred, end is the time at which the sample reached the surface.

We show further modeling parameters and the results for the best fit model computed with PyBasin (Fig. 9). For more detail, we also present closeups for the younger history and a shorter AHe age time frame (Fig. 9.1, 9.2). Surface temperatures for times older than 45 Ma are taken from Mazurek et al. (2006) and adjusted for expected water depths (Fig. 9a). We assume a temperature profile for tropical regions (Ward, 2006) and estimate water depth by facies extracted from the lithostratigraphic log of the Bülach well (Nagra, 2020). After 45 Ma, we use surface temperatures of Mosbrugger et al. (2005). The burial plot shows the subsidence phases determined by stratigraphic ages (Kämpfen, 1972) and drilled thicknesses (Fig. 9b, Nagra, 2020). By testing a range of values in separate model runs, we explored the amount of additional sedimentation and

subsequent erosion that fits best to the AHe ages. For the best fit, we arrived at 400 m of sedimentation between the Upper Jurassic and 65 Ma, which we define to be subsequently eroded by an exhumation event from 65 to 50 Ma. Evidence for this is the maximum of 400 m of Cretaceous sediments preserved in synclines of the Jura fold-and-thrust belt (Strasser et al., 2016), as well as the same amount of maximum Cretaceous sediments farther east in the Molasse Basin (e.g., Ortner et al., 2015). The uppermost Jurassic formation (Felsenkalk/Massenkalk) is preserved in the section drilled in the Bülach well, indicating that negligible amounts of Jurassic strata have been eroded (Nagra, 2020).

lithology	density [kg/m³]	surface porosity	compr. [m^{-1}]	thermal cond. [W/(m*K)]	heat capacity [J/(kg*K)]
conglomerate	2650	0.20	0.000395	4.80	2800
sand	2650	0.20	0.000395	4.80	2800
silt	2700	0.25	0.000395	3.50	2500
clay	2650	0.15	0.000900	2.50	2100
limestone	2750	0.05	0.000790	2.90	2600
dolomite	2850	0.30	0.000790	4.80	2600
marl	2650	0.20	0.000790	2.70	2400
anhydrite	2900	0.10		5.50	900
halite	2100	0.05		5.50	900
coal	2650	0.05		1.00	900
water	1025			0.65	4181

Table 3. Rock properties of the different lithologies. Density, surface porosity and compressibility derived from measurements on the Bülach drill cores (Nagra, 2020). Thermal conductivity and heat capacity from measurements on the Weiach drill cores (Mazurek et al., 2006).

For the Molasse stage, best fits are obtained with 1100 meters of additional sedimentation and subsequent erosion, which is in agreement with the estimate of a paleo PRZ just below 600 m (Fig. 2). The additional sedimentation requires slightly higher sedimentation rates after 17 Ma (Fig. 9). Using maps and cross-sections of the Bülach region (Haldimann et al., 2017), we separate these 1100 meters of additional sedimentation to different stratigraphic units. We define 50 more meters of USM II, 100 meters of OMM and 950 meters of OSM. The precise time span of the exhumation event is the result of modeling incremental changes to the onset and end of exhumation, with the best fit obtained for the start at 11 Ma and an end at 0 Ma.

In addition to the burial and exhumation history, the pre-depositional provenance histories of the grains are defined for each stratigraphic unit (Fig. 9b, 9.1, yellow fields). These provenance paths are based on the exhumation history of the Alps (e.g., Hurford, 1986; Schmid et al., 2004; Glotzbach et al., 2011a; Egli et al., 2017a; Herwegh et al., 2017; Kissling and Schlunegger, 2018; Herwegh et al., 2020) in possible provenance regions (e.g., Spiegel et al., 2001; Kuhlemann and Kempf, 2002; Berger et al., 2005b). Heat flow development through time can be freely adjusted (Fig. 9c). We account for heat flow

histories as proposed by previous studies (e.g., Mazurek et al., 2006; Omodeo-Salé et al., 2021) and adjusted these for the best fit to our data. The present-day heat flow is determined by the measured borehole temperatures. This temperature profile as measured in the Bülach well (Nagra, 2020) is shown in Figure 9d. Depositional age of strata and AHe ages of all grains are plotted in Figure 9e and 9.2.
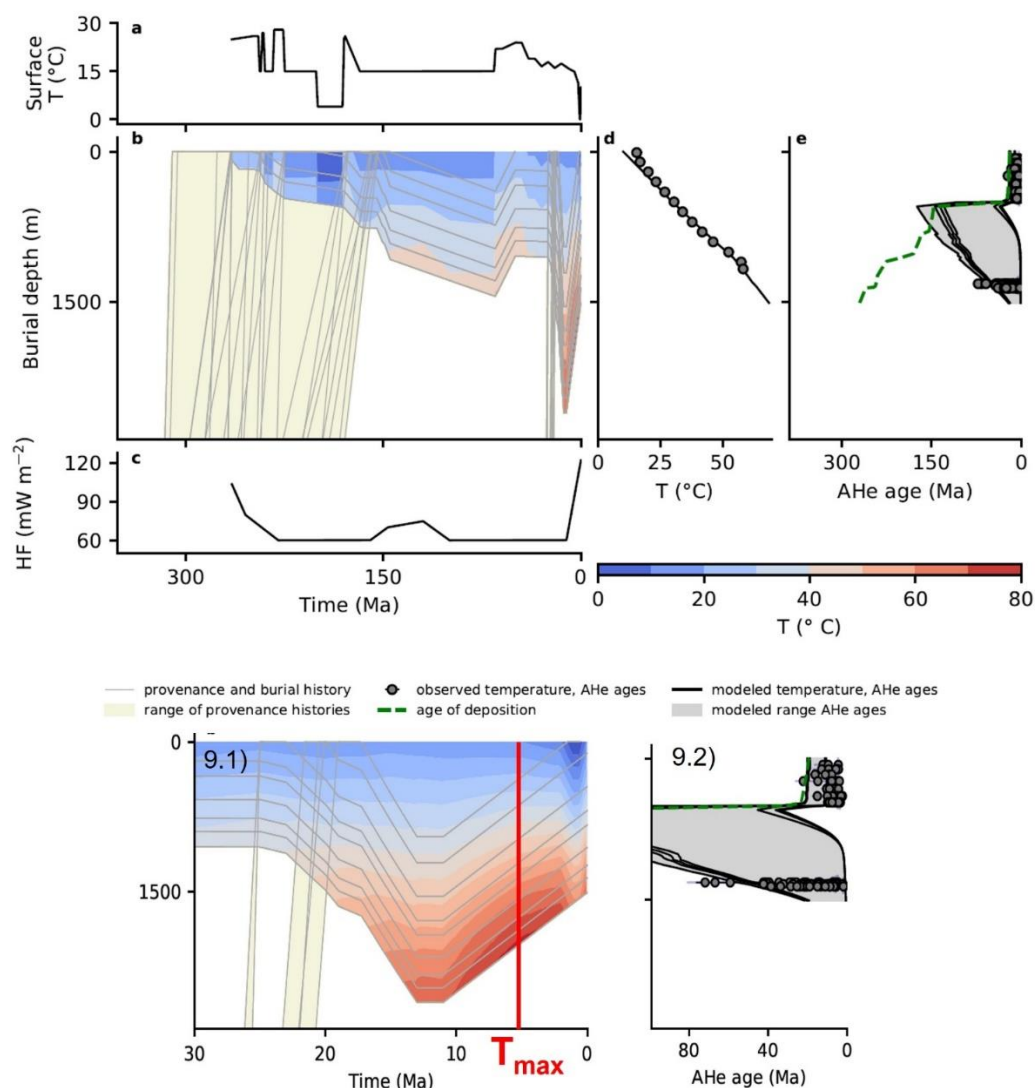
Figure 9. PyBasin model parameters and results for the best fit model using all samples (MOL1 – RL2). a) surface temperature over time (after Mazurek et al., 2006; Mosbrugger et al., 2005). b) burial plot including preserved stratigraphic column (Nagra, 2020) and additional sedimentation and erosion defined manually. Colors of the burial plot give temperatures of each stratigraphic unit with time, calculated by PyBasin. Yellow areas are provenance history paths. c) basal heat flow over time based on previous studies, and adjusted to provide the best fit to the data. d) measured borehole temperatures of the Bülach well (Nagra, 2020) and modeled temperature profile. e) AHe age data, stratigraphic ages and modeled AHe ranges. Figure 9.1. closeup of the burial plot with time axis limitation to 30 Ma. Maximum temperature (Tmax) is calculated at 5 Ma, during ongoing exhumation because of rising heat flow. Figure 9.2. closeup of the AHe age panel, age axis is cut at 90 Ma.

The depth vs. present day temperature plot (Fig. 9d) shows that the calculated temperature profile matches measured
530 borehole temperatures, with a deviation of measured data to higher temperatures in the Molasse section (upper 500 m).
Figure 9b shows the modeled temperature history plotted as heat map into the burial plot. Maximum temperatures were
reached during exhumation at about 5 Ma, as increasing heat flow has a larger effect than cooling by erosion. PyBasin
computes theoretical AHe age ranges for all defined provenance paths. These calculated AHe age ranges explain all
Buntsandstein and Rotliegend data well, apart from the three oldest grains measured (<5% of the data) (Fig. 9e and 9.2). The
535 excursion of the expected AHe age range to young ages for the Molasse grains is also backed by the model. Still, for the
Molasse section, only AHe ages older than 15 Ma are explained. We account for this in the following refined model for the
Molasse section and discuss possible reasons later.

4.5.2 Refined model for the Molasse sequence

540 We modeled the Molasse sample and time interval separately for a fit to the so far unexplained young AHe ages and to arrive
at a more detailed thermal history of the basin. Input parameters are equal to those of the best fit model (Fig. 9), if not stated
differently in the following. Exploring the settings fitting best to the data, we arrive at a two-stepped exhumation approach
starting at 13 Ma (Fig. 9b). We define accelerated exhumation that starts at 9 Ma and lasts until today. Previous studies and
our best fit model for all sampling intervals propose a sharp increase of heat flow from around 10 Ma to recent times (e.g.,
545 Mazurek et al., 2006; Omodeo-Salé et al., 2021) (Fig. 9). To explore parameter space with a setting not needing such a sharp
increase, we set the heat flow to 122 mW/m² throughout the whole Molasse stage instead of rising to this magnitude to
recent times (Fig. 10c). Also, we allow a provenance history path of Variscan initial exhumation (cooling below 120 °C) in
order to account for oldest AHe ages. The exhumation magnitude is decreased to 1000 m compared to the previous model as
this provides a better fit following the changes to the heat flow and provenance histories.

550

The modeling result shows increased temperatures during Molasse burial, related to the elevated heat flow and buffered by
100 m of less maximum burial (Fig. 10b). Maximum temperatures of close to 80 °C are now reached at maximum burial at
around 13 Ma. The deviation of modeled borehole temperatures from the measured temperatures to shallow depth can be
observed as for the best fit model (Fig. 10d). As an effect of the adjustments, most of the data is now explained by the
555 modeled range of AHe ages (Fig. 10e). The newly introduced provenance path with exhumation beginning in Variscan times
explains the oldest grains. Geologic reasoning for these assumptions providing a good fit will be discussed later. In the
following, we test robustness and uncertainties of our models to explore the error bar related to our parameter settings.

560
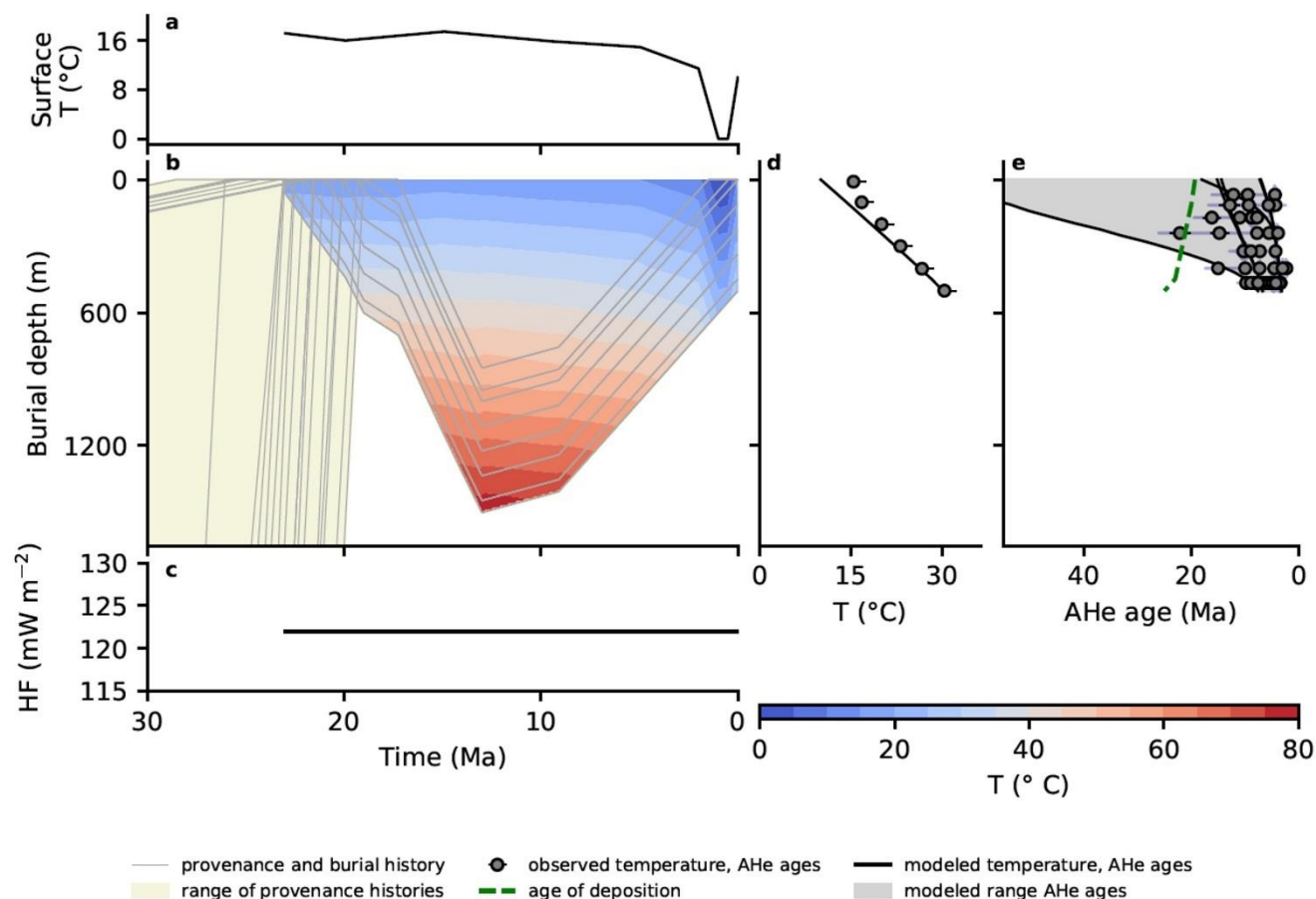
Figure 10. PyBasin model parameters and results for the refined Molasse model using samples MOL1 – MOL7. For panel explanations see Fig. 9.

4.5.3 Exploring parameter space with PyBasin

565 To test the sensitivity of the modeled AHe age ranges and the robustness of the best fit, we run models in which we change one parameter at a time by a small increment. The base model for these tests is the best-fit model for all sampling intervals (Fig. 9). The resulting AHe age ranges of the base model are presented again in Figure 11a. We change burial and subsequent exhumation magnitude of the Molasse stage exhumation by 200 m. In a first test we add 200 m, i.e., 1300 m of burial and subsequent exhumation (Fig. 11b). Second, we test the influence of 200 m less exhumation (900 m, Fig. 11c).

570 Compared to the best fit model (Fig. 9) the computed AHe age ranges for the lower sample sets (BST-RL) are very sensitive to the 200 m difference of exhumation (Fig. 11b, 11c). Adding 200 m of sedimentation and subsequent erosion increases the maximum temperature and thus decreases the expected AHe ages (Fig. 11b). Due to this, about the oldest third of BST-RL

AHe ages is not explained by this model. Reducing burial/exhumation by 200 m results in colder maximum temperatures
(Fig. 11c). This increases the computed AHe age range. As a consequence, about 20 Ma older AHe ages are expected by this

575   model than most of the oldest data suggests. The computed theoretical AHe age range for the Molasse samples is less
sensitive to the 200 m changes in exhumation magnitude (Fig. 11b, 11c). Less exhumation shifts the limits of computed age
ranges about 1-2 Ma to older ages. For more exhumation, 1-2 Ma younger AHe ages are computed.

b&h mag.: base	b&e mag.: **+200 m**	b&e mag.: **-200 m**	b&h mag.: base	b&h mag.: base	b&h mag.: base
b&h t(start): base	b&h t(start): base	b&h t(start): base	b&h t(start): **-1 Ma**	b&h t(start): **+1 Ma**	b&h t(start): base
HF: base	HF: base	HF: base	HF: base	HF: base	HF: **+10%**
Prov. ages: base	Prov. ages: base	Prov. ages: base	Prov. ages: base	Prov. ages: base	Prov. ages: base
a)	b)	c)	d)	e)	f)

b&h mag.: base	b&e mag.: **-200 m**	b&e mag.: **+200 m**	b&e mag.: **-200 m**	b&h mag.: base	b&h mag.: base
b&h t(start): base	b&h t(start): base	b&h t(start): base	b&h t(start): base	b&h t(start): base	b&h t(start): base
HF: **-10%**	HF: **+10%**	HF: **-10%**	HF: **+10% (MOL)**	HF: base	HF: base
Prov. ages: base	Prov. ages: base	Prov. ages: base	Prov. ages: base	Prov. ages: **+10%**	Prov. ages: **-10%**
g)	h)	i)	j)	k)	l)

580   **Figure 11. AHe ages and modeled AHe age ranges for different scenarios diverging from the base of the best fit model presented in
Fig. 9. b&e mag.: burial and exhumation magnitude. b&h t(start): timing of onset of Molasse stage exhumation that lasts until
recent times, where – 1Ma means a start 1 Ma earlier. HF: heat flow over the complete modeled time-span, where +10% means
10% higher heat flow for each data point (except recent HF), 10j: HF +10% only for the Molasse stage (MOL, last 30 Ma). Prov.
Ages: provenance ages, where +10% means that provenance history exhumation is 10% of absolute date earlier for each**

585   **population, resulting in older provenance ages.**

We also test changes to the onset of exhumation, in particular one Ma earlier (12 Ma, Fig. 11d) and one Ma later (10 Ma,
Fig. 11e). As for the base model, maximum temperature is reached on the exhumation path (Fig. 9). In the model where
exhumation starts one Ma earlier, this maximum temperature is lower as compared to the best fit model. The opposite effect

590   occurs for a later start of exhumation. Oldest BST-RL ages are not explained by the model with a later start of exhumation
      (Fig. 11d), while an earlier start of exhumation leaves a range of older AHe ages that is not backed by data (Fig. 11e).
      However, the impact on theoretical Molasse AHe ages is minor. Generally, changing the exhumation magnitude by 200 m
      has a larger effect on the computed AHe ages than changing onset of exhumation by 1 Ma.

595   Next, we explore the influence of heat flow. In a first experiment, we add 10% to the heat flow for all defined points in time
      (Fig. 11f) and subtract 10% in a second experiment (Fig. 11g). Only the present day heat flow is kept at 122 mW/m², as this
      needs to correspond to the recent borehole temperature profile (Nagra, 2020). Increased basal heat flow increases
      temperature, especially for the sample sets near the base. This means adding 10% of heat flow affects the computed BST-RL
      AHe ages most. Around 40% of the BST-RL data is thus no longer explained, while the effect on Molasse AHe ages is small
600   (Fig. 11f). Decreasing the basal heat flow consequently allows for much older AHe ages of BST-RL section. Up to 30 Ma
      older ages than obtained by our measurements are calculated (Fig. 11g). Molasse AHe ages increase slightly to that extent
      that all ages measured in interval MOL7 would be younger than the theoretical AHe age range. Changing exhumation
      magnitude by 200 m and changing heat flow by 10% results in comparable changes to the computed AHe age ranges (Fig.
      11b, 11c, 11f, 11g). The main difference is that changing the exhumation magnitude affects all samples along the well,
605   relative to the computed absolute ages. A change in heat flow has its largest impact near the base of the model.

      As changes in heat flow and burial and exhumation are the main drivers of temperature changes, we test the effects of
      exchanging both for each other. Starting from the base model, we compute one model with the heat flow increased by 10%
      and Molasse burial and exhumation decreased by 200 m (Fig. 11h). The second model uses a heat flow decreased by 10%
610   and 200 m more burial and exhumation (Fig. 11i). As shown by the resulting theoretical AHe age ranges, the heat flow
      change is slightly dominant for the BST-RL sample set, as it governs a minor shift of the AHe age ranges (Fig. 11h, 11i). In
      contrast, theoretical AHe ages for the Molasse part are dominantly affected by the exhumation change. Rising heat flow but
      decreasing exhumation creates a worse fit to the Molasse AHe data. This is not only because basal heat flow affects lower
      samples more, but because we apply a change to the heat flow over all the modeled time span. This results in a first influence
615   on the BST-RL data with different peak temperatures around 65 Ma. To buffer this effect, we set up a model with 10%
      increased heat flow only in the Molasse stage (Fig. 11j). The change in computed AHe age ranges for the BST-RL section is
      minor, indicating that the deeper and hotter burial phase of the molasse stage has a dominant effect on AHe ages.

      The influence of provenance ages is tested by shifting these by 10% to older times (Fig. 11k) and younger times (Fig. 11l).
620   There is a logical limit as the exhumation in the source region needs to take place before deposition. In cases where the end
      of this source region exhumation could not be shifted to younger times, we still shift the onset to 10% later. This results in
      faster exhumation and should reduce provenance AHe ages. A shift of the provenance region exhumation means adding time

between cooling of the grains in the source region and reheating after deposition. This results in more initial helium concentration in the grains before reheating and subsequently higher theoretical AHe ages.

625

Summarizing, the models are sensitive to minor changes of exhumation and heat flow. 200 m of change to the exhumation magnitude causes a shift of modeled AHe age ranges by around 20 Ma (Fig. 11b, 11c). Exchanging heat flow for burial and exhumation seemingly allows for more freedom of the exhumation magnitude but higher heat flow and less exhumation cannot explain the higher temperatures needed for the Molasse AHe data (Fig. 11j). Lowering the basal heat flow and adding

630 exhumation produces better fits to the Molasse data, but heat flow values below 55 mW/m² are far off the range explored by previous studies on the heat flow history of the basin (e.g., Schegg and Leu, 1998; Mazurek et al., 2006; Omodeo-Salé et al., 2021). Following this, we estimate the uncertainty on the exhumation magnitude to be 100 m at maximum. Considering the refined model for the Molasse sequence as well, we conclude an exhumation magnitude estimate of 1050 m +/- 100 m.

635 ### 4.5.4 Bülach vitrinite reflectance data

PyBasin allows the inclusion of vitrinite reflectance (VR) data. We use VR data measured on the Bülach drill core and present a model including both, VR and AHe (Fig. 12). This model fits the computed VR trend to the highest values measured in both respects, magnitude and gradient of VR data (Fig. 12e). We need 4 km of additional Upper Jurassic and Cretaceous burial and subsequent exhumation to arrive at this fit, compared to the base model (Fig. 9). This is an

640 unrealistically high number, in conflict with stratigraphic constrains (see above). Increasing the heat flow can only be done to a limited extent, as the VR data shows a shallow gradient which increased heat flow would not allow. The resulting increased temperatures would be in conflict with the older half of the AHe ages measure in the BST-RL section. In summary, VR data requires additional explanations, as it either requires unrealistic amounts of Mesozoic sedimentation or heat flow values in conflict with only partially reset AHe data and VR data gradients. We discuss a possible scenario

645 explaining these contradictions as a separate point below.
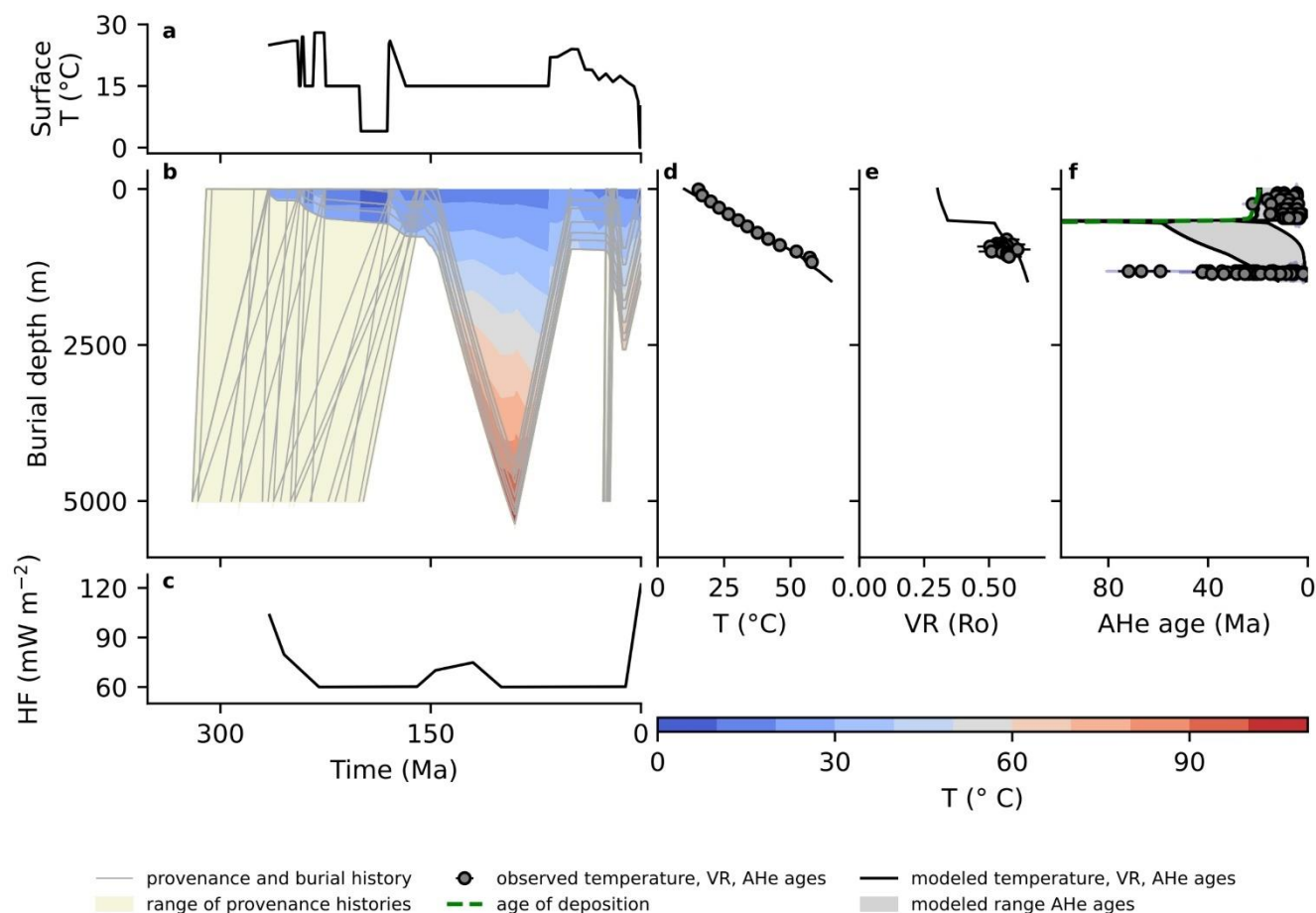
Figure 12. PyBasin model with consideration of VR data measured on samples from the Bülach drill core. For panel explanations, see Fig. 9, except e) here VR data (dots) and the modeled expected VR values for the given thermal history. f) AHe data and modeled AHe ages, as panel e in Fig. 9.

5 Discussion

5.1 Comparing the modeling tools HeFTy, QTQt and PyBasin

We have used a vertical section and a large amount of single grain age (U-Th-Sm)/He data to reconcile previous hypotheses on uplift and exhumation of the foreland basin of the Central Alps. To constrain this thermal history, we use HeFTy (Ketcham, 2005) and QTQt (Gallagher, 2012), as well as PyBasin (Luijendijk et al., 2011). We show that HeFTy is useful to model single grains or smaller groups of grains with similar AHe ages, testing different constraints or diffusion models. We show that using HeFTy, it is possible to produce good fitting models for separate groups of Molasse grains. However, bringing these together to a single temperature history leaves a wide range of cooling magnitudes, timings, and rates (Figs. 5, 6). This is partly because parameters such as basal heat flow and surface temperature cannot vary with time. For rock

properties, average values for the whole stratigraphic pile can be set only. Building a vertical profile of rock properties
660 resembling the actual rock sequence is thus not possible. The results are inaccuracies in the computed temperature profile,
especially for sequences containing evaporites or coal because of their exceptional thermal conductivity. Additionally, for
our data including partially reset samples in sediments, different provenance histories within a single sample set are
expected. As HeFTy computes a single temperature path for all grains integrated in a single model run, possibly differing
pre-depositional thermal histories are not considered. This makes it difficult to find good paths, as these try to fit an average
665 provenance history in this case. Also, HeFTy tends to favor paths where complete reset of the grains took place, which is not
applicable for all grains in our data set. In summary, HeFTy modeling has been powerful for highlighting complications
within the data set, guiding further modeling directions. For explaining the data set and in particular testing the influence of
different parameters such as heat flow or rock properties, additional modeling approaches were necessary.

670 QTQt (Gallagher, 2012) can be used to model sample sets of many grains, which is useful to find common time-temperature
paths for a whole set of available data. However, problems occur when attempting to model our full complex dataset with
QTQt. When recent temperatures are constrained, the offset or temperature difference observed after rapid cooling around 12
Ma is not well resolved, as illustrated by the non-parallel 95% credible intervals of the uppermost and lowermost samples
(Fig. 5a). Not constraining the recent temperature profile results in a model that does not show diverging cooling paths.
675 However, this model implies a too low recent geothermal gradient of around 5 °C/km, which illustrates the high degree of
inconsistency modeling both sample sets together (Fig. 7b). The probabilistic models generated by QTQt show that
especially the models for the BST-RL sequence leave a broad range of equally viable possibilities (Fig. 8). These problems
could be related to different factors. (1) the data provide too little information regarding the young part of the thermal history
path (Gallagher, 2012). Thus, the young thermal history cannot be well constrained, because the output of QTQt is
680 conditional on the input data (and their assumed uncertainties), and the assumed range or domain of possible values for the
thermal histories themselves (Gallagher and Ketcham, 2018). (2) QTQt cannot take rock properties as input parameters.
Consequently, effects on the thermal regime imposed by stratigraphy will be missed. (3) It is not possible to account for
provenance ages using QTQt. Disregarding these, the AHe ages of the BST-RL sample set are difficult to explain. (4) QTQt
cannot account for changes in heat flow over time. Both, HeFTy und QTQt model temperature over time only. Thus, they
685 only consider heating and cooling. This is not necessarily translatable to exhumation, as a change in heat flow is the other
parameter capable of producing heating and cooling events.

PyBasin can handle many grains in a single model, and it can account for different provenance thermal histories.
Exhumation and heat flow histories can be adjusted independently. In this way, it is possible to build a single consistent
690 thermal history model for a complex dataset that even shows older AHe ages to depth (Fig. 3, 9). The computed heat map on
the burial plot shows when heating and cooling takes place, independent of exhumation or burial stages (Fig. 9b, 9.2, 10b).
Furthermore, the forward modeling approach of PyBasin allows to explore sensitivities and robustness of the results to

changes of different parameters. However, exhumation paths in PyBasin are limited in the way that constant rates are assumed between defined starts and ends to exhumation phases. This can be circumvented by splitting exhumation events in

695   two or more steps of different rates.

5.3 Comparison to VR data

VR data seemingly disagrees with AHe data (Fig. 12, 13). It either suggest unrealistically high Cretaceous burial, or alternatively, unrealistically high Molasse sedimentation and subsequent exhumation. We suggest that hydrothermal events,

700   probably related to Jurassic rifting, as discussed for example by Timar-Geng et al. (2004), cause VR data to show higher maturation than expected by basal heat flow (Fig. 13). The shallow gradient of VR data supports this hypothesis, as only hydrothermal heat allows for such shallow VR gradients at this level of maturity in shallow depths. The AHe system is not affected by these hydrothermal shocks as it is not sensitive enough to short temperature peaks. Alternatively, the BST-RL sequences where sealed from the hydrothermal influence by Triassic evaporites between these sediments and the Jurassic

705   sequences that host VR data. Alternatively, VR data is subject to reworked vitrinites that inherit maturation values of their source region.

5.4 Implications on the thermal history of the northern Swiss Molasse Basin

The constraints of the thermal history of the northern Swiss Molasse Basin are based on a set of measurable parameters as

710   the recent temperature profile, rock properties and thermochronometric datasets as compiled in this study. Based on these boundary conditions, we narrowed down provenance, heat flow and burial and exhumation histories to find a consistent thermal history. In the following, we discuss key parameter constraints made and derive implications arising from the final thermal history models.

715   Modeling shows that provenance history seems to be key for understanding the spread in ages. The older ages of the BST-RL sequence compared to the Molasse section can only be explained the Permo-Carboniferous provenance ages of BST-RL grains and the long time spent at relatively low temperature prior to Molasse sedimentation (Fig. 9). Most Molasse grains have young provenance ages as they got exhumed in the rising Alpine chain shortly before deposition in the basin (e.g., Hurford, 1986; Schmid et al., 1996; Spiegel et al., 2001; Kissling and Schlunegger, 2018). However, the refined model for

720   the Molasse sequence (Fig. 9) shows that oldest AHe ages indicate a population of older provenance ages than expected for Alpine exhumation. A possible source region for such grains is the Black Forest (e.g., Timar-Geng et al., 2004; Spiegel et al., 2007; Meyer et al., 2010). Paleogeographic and paleo-drainage studies show that possible provenance regions for Molasse sediments of the study area are the Alpine chain from as far west as the recent location of Lake Geneva, as well as sediments derived from the Black Forest region (Fig. 1; e.g., Spiegel et al., 2001; Kuhlemann and Kempf, 2002; Berger et al., 2005b).

725

We arrive at a single mutually consistent thermal model, but the best fit model leaves youngest AHe ages of the Molasse sequence unexplained (Fig. 9). Consequently, for resolving the double-PRZ pattern of the dataset, provenance age alone is not sufficient. One possible solution might root in exceptionally high closure temperatures for the BST-RL grains that is not expected by modeling algorithms. In recent years, more attention was focused on the relevance of the radiation damage on

730 increasing the AHe closure temperature, reaching temperatures >100°C (e.g., Flowers et al., 2022). We tested HeFTy and QTQt models using RDAAM as diffusion model, which did not have an effect on the resulting models (see above). With PyBasin (Luijendijk et al., 2011), we account for high closure temperatures, as old provenance ages imply a high radiation damage density and a high initial helium concentration prior to re-heating (Shuster et al., 2006; Flowers, 2009). Radiation damage (Flowers, 2009) and helium concentration (Shuster et al., 2006) are considered as proxies for closure temperature.

735 Consequently, we propose that inconsistencies are not a problem of understanding the AHe system and diffusion models. Instead, we argue for a more complex thermal history than could be resolved with previous data sets.

For the best fit to our data, we need a sharp increase in basal heat flow from 60 mW/m² at 11 Ma to reach its present day magnitude of 122 mW/m². Starting this heat flow increase earlier would cause temperatures at maximum burial to be too

740 high to explain the AHe ages measured for the BST-RL sequence. This sharp increase has been proposed in previous studies (e.g., Mazurek et al., 2006; Omodeo-Salé et al., 2021). However, such an event needs an underlying geologic process and evidence.

Complex heat flow settings have been recognized for other basins globally. For the North Slope of Alaska, local heat flow

745 variations by a factor of three have been detected, which are explained by basin-scale groundwater flow (Deming et al., 1992). A comparable setting is interpreted for the Western Canada Sedimentary Basin (Weides and Majorowicz, 2014). Uniform basal heat flow effects of hydrothermal systems are reported for the Foreland Basin south of the Alps in northern Italy (Pola et al., 2020). However, these examples discuss spatial, not temporal variations of heat flow. Temporal heat flow changes have been analyzed for German Variscan basins, heat flow values between 50 mW/m² and 70 mW/m² are proposed

750 for burial in Carboniferous times, with predating values up to 110 mW/m² during Early Devonian rifting, associated with volcanism (Littke et al., 2000).

For the region of the northern Swiss Molasse Basin, several drivers for heat flow changes through time may exist. First, between 15 and 7 Ma, the Hegau volcanic system was active, as witnessed by ash layers in the Molasse sediments. Volcanic

755 activity, possibly associated with a mantle source may have cause local flux of hydrothermal fluids and generally elevated geothermal gradients (Hofmann, 1975; Schreiner, 1992; Rahn and Selbekk, 2007). Furthermore, elevated heat flow may be caused by Plio-Pleistocene reactivation of basement faults related to the European Cenozoic rift system (Giamboni et al., 2004; Mazurek et al., 2006), or heat transport along basement faults (Griesser and Rybach, 1989; Mazurek et al., 2006).

760 These effects have also been proposed for other foreland basins worldwide (e.g., Deming et al., 1992; Weides and Majorowicz, 2014; Pola et al., 2020).

Recognizing the modeled AHe ages for the Molasse samples that do not explain the youngest measured ages, we offer a refined model of the Molasse sequence that avoids the sharp increase in basal heat flow but uses the elevated basal heat flow of 122 mW/m² throughout the entire time span from burial to exhumation (Fig. 10). As explained above, such a high basal 765 heat flow at maximum burial would cause too high temperatures to explain to BST-RL age data. Consequently, we do not consider basal heat flow from below the BST-RL sequence. Instead, we need a heat source that affects the Molasse sequence but not the BST-RL sequence. This is possible with migration of hydrothermal fluids focused in the Molasse sequence. In this case, the BST-RL and Molasse sequences need to be hydrologically decoupled and flow of hot fluids into the Molasse. Measured borehole temperatures deviate from the modeled temperatures to higher values towards the surface (Figs. 9, 10). 770 This requires that additional heat compared to that modeled by basal heat flow and heat conduction through the rock is present in the uppermost sequence. Recent hydrothermal systems exist in the study area showing the availability of hot fluids in the shallow subsurface, such as observed in the Baden and Schinznach hydrothermal system (Luijendijk, 2019). We speculate that the Middle Jurassic Opalinus Clay and adjacent marls may serve as a hydrologically decoupling horizon between the Molasse and BST-RL sequences (Fig. 2, 3). The unit has been shown to have and exceptionally low hydraulic 775 conductivity (Nagra 2020) and represents a rheologically weak layer capable to tectonically decouple the more competent Mesozoic rocks above and below (e.g., Roche et al., 2020). Alternatively, the Triassic evaporites (Fig. 2) have also been shown to be an effective decoupling horizon (Jordan, 1992; Burkhard and Sommaruga, 1998).

5.5 Evaluation of the Bülach constraints in the context of previous studies

We consider the Bülach-1 well to be representative for the region of the Northern Swiss Molasse Basin, as stratigraphy and 780 measured recent borehole temperatures are comparable with those of other nearby wells (e.g., Mazurek et al., 2006; von Hagke et al. 2015). Also, no major tectonic structures of considerable offset and/or throw affect the well and the closer area, which rules out local exhumation contributions. Previous studies obtained different results on exhumation magnitude and timing of the northern Swiss Molasse Basin. Mazurek et al. (2006) argue for 750 m – 1050 m since 9 Ma, while Cederbom et al. (2011) argue for 800 m – 1600 m since 5 Ma. Indeed, the data allows for a broad spectrum of exhumation scenarios with 785 onset ages ranging at minimum from 4 Ma to about 12 Ma (von Hagke et al., 2015). We present a model considering all data with a best fit of about 1100 m of exhumation since about 11 Ma. Our refined model for the Molasse stage proposes slow exhumation from 13 to 9 Ma and accelerated exhumation since 9 Ma, resulting in a sum of 1000 m of exhumation. These constraints are not only comparable to the results of Mazurek et al. (2006), our models also explain the results of Cederbom et al. (2011). As discussed above, standard modeling tools for thermochronologic data analyze heating and cooling, without 790 distinguishing between burial and exhumation or heat flow effects. The authors state that they assume constant heat flow over time to arrive at their conclusion. Our results show that due to the increasing heat flow starting at 11 Ma, maximum

temperatures are reached around 5 Ma, despite exhumation starting at 11 Ma (Fig. 9). This is also supported by clumped isotope data that indicate that no cooling occurred before 4.5 Ma (Looser et al., 2021). Hence, we agree with Cederbom et al. (2011) and Looser et al. (2021) to the extent that cooling started at around 5 Ma, while erosion may have started already
795 earlier and contemporaneously with uplift and exhumation reported from the Subalpine Molasse (von Hagke et al. 2012, 2014; Mock et al. 2020), as well as with thrusting in the Jura Mountains (Laubscher, 1978; Philippe, 1996).

5.6 Processes driving exhumation

Previous studies proposed climatic, tectonic, or geodynamic drivers of exhumation, or a combination thereof (see above).
800 We evaluate these contributors in the light of our constrained exhumation history of 1050 +/- 100 m starting at 13 Ma, accelerating at 9 Ma. Tectonic events affecting the study area are related to folding of the Jura fold-and-thrust belt, both uplift of the basin during passive transport above a thin-skinned décollement, as well as local uplift associated with individual faults (Laubscher, 1978; Jordan et al., 2015). Jura folding started in its southern parts possibly as early as 14 Ma (Looser et al., 2021), or around 12 Ma the latest (Sommaruga et al., 1997; Burkhard & Sommaruga, 1998; Becker, 2000).
805 Since then, deformation propagated northwards, and possibly is still active, however in a thick-skinned fashion (Giamboni et al. 2004; Madritsch et al. 2010). Structures possibly associated with early Jura folding are present in the study area and drilled in the Bülach well (Nagra, 2020). We speculate this this tectonic exhumation accounts for the slow starting phase of exhumation we propose from 13 Ma on (Fig. 10). However, the magnitude of tectonic contribution can only be low, as structures drilled and mapped in reflection seismic data account for a maximum of 100 m of exhumation (Malz et al., 2016;
810 Haldimann et al., 2017; Nagra, 2019; Nagra, 2020).

Climatic drivers are twofold. First, exhumation associated with Quaternary glaciations. Glacial scouring, incision of subglacial channels and isostatic rebound after glaciation affected the study area (Haldimann et al., 2017; Buechi et al., 2018; Pollhammer et al., 2022). It can however not account for exhumation recorded by our data that has long been ongoing prior
815 to Quaternary glaciation. Second, global climate changes, and particularly increased erosion since approximately 5 Ma have been proposed for mountain belts all over the world (e.g., Molnar & England, 1990; Herman et al. 2013), as well as the Alpine foreland (Cederbom et al. 2004, 2011; Champagnac et al. 2009). However, the global increase of erosion rates associated with climate change has been questioned (e.g., Willenbring and von Blankenburg, 2010; Ganti et al., 2016; Schildgen et al., 2018). Similarly, thermochronological data of the Molasse Basin do not necessarily require a single
820 exhumation pulse at 5 Ma (von Hagke et al. 2012, 2015). Our data set does not support an exhumation pulse starting as late as 5 Ma, because in this case, BST-RL ages would require total reset. While we cannot completely rule out climate as a driver, its influence is not required to explain existing data.

Last, geodynamic processes such as slab rollback, delamination or breakoff can result in foreland basin uplift in general, and
825   in the case of the Alpine foreland in particular (e.g., Lyon-Caen and Molnar, 1989; Lippitsch, 2003; Genser et al., 2007; von
Hagke et al. 2012; Schlunegger and Kissling, 2015; Herwegh et al., 2017; Baran et al. 2014). Such processes are
characterized by large wavelength uplift and exhumation lasting over several millions of years. Typically, they are associated
with volcanic activity and drainage reorganization (e.g., Braun et al., 2014; Robl et al., 2017). In the north Alpine foreland
basin, both, volcanic activity, as well as drainage reorganization of the Rhine River has been observed since the Late
830   Miocene (Hofmann, 1975; Schreiner, 1992; Rahn and Selbekk, 2007; Kuhlemann and Rahn, 2013; Yanites et al., 2013).

We propose a model, where all drivers may be active, however to variable degree. Early exhumation at 13 Ma may be
associated with early Jura folding. The main exhumation phase starting at 9 Ma does not coincide with a climatic event, but
roughly fits with timing of Hegau volcanism. Consequently, we relate this phase with geodynamic processes. These may also
835   be responsible for later drainage reorganization and further exhumation. A last phase of cooling may be associated with
glacial processes; however, their contribution to exhumation is not resolved with our data set and would need specific
studies, e.g. applying terrace morphometry.

6 Conclusions

We show that dating many grains in dense sampling intervals with apatite helium thermochronometry is a suitable method to
840   reconcile and better constrain the burial and exhumation history of the northern Swiss Molasse Basin. Our single grain age
dataset shows a counterintuitive pattern, where the upper Molasse samples may imply total reset below 600 m, while ages
from Permo-Triassic samples at more than 1300 m depth are not reset. We show that by including rock properties,
exhumation history, changes in basal heat flow, and especially provenance ages into the models, consistent thermal histories
can be obtained from this dataset.

845

Reconciling previous works, we arrive at an exhumation estimate of 1050 +/- 100 m of late Miocene exhumation. We
propose slow exhumation beginning as early as 13 Ma, with accelerating exhumation rates at 9 Ma. Our models also show
that cooling starts as late as 5 Ma, despite an earlier start of exhumation. This is because rising heat flow since 11 Ma causes
heating until 5 Ma. We consider this discrepancy as a reason for contradicting previous studies, when cooling and
850   exhumation are not distinguished. The magnitude and timing estimates of this study are robust, not only by the statistical
robustness of the dataset, but also because of the high degree of sensitivity of PyBasin models to small changes in parameter
settings. Also, we consider the Bülach well as representative for the northern Swiss Molasse Basin, because borehole
temperatures are similar to those of nearby wells and no tectonic structures accommodating large offsets exist that could
account for local exhumation scenarios.

855

We propose that additional heat by hydrothermal activity explains the youngest Molasse AHe ages that provenance age alone cannot account for. Deviating measured temperatures from the modeled profile indicate that additional heat on top of the heat rooted in basal heat flow is present. This is also supported by the presence of thermal springs in the area. The Middle Jurassic Opalinus Clay or Triassic Evaporites can serve as hydrologically sealing horizons between the Molasse and

860 BST-RL sampling intervals. This finding implies that hydrothermal activity or heat flow events in general can be confused with exhumation, which is a challenge for constraining exhumation using thermochronometry.

We assume geodynamic processes are the main driver of exhumation, as these can account for an exhumation onset earlier than 5 Ma. We consider reorganization of the Rhine River drainage system from 4.2 Ma being a symptom of this ongoing exhumation process. Tectonic forcing of exhumation associated with the onset of folding in the Jura fold-and-thrust belt

865 could have played a role in the slow onset of exhumation from 13 Ma. The role of Miocene climate changes on basin wide exhumation seems to be minor. The Influence of Quaternary glaciations cannot be seen in our data, and requires additional studies using different methods.

7 Author contributions

Frings, K. A.: sampling, sample processing, thermochronometric data processing, all modeling

870 Luijendijk, E.: PyBasin modeling

Dunkl, I.: thermochronometric measurement, thermochronometric data processing, HeFTy modeling

Villamizar-Escalante, N.: QTQt modeling

Madritsch, H.: conceived the study, sampling, data processing

von Hagke, C.: conceived the study, model conception

875 All authors contributed to discussions and writing the text. This study is part of the SANDS project funded by Nagra and the Geological Institute of RWTH Aachen University

9 Competing interests

The authors declare that they have no conflict of interest.

10 Acknowledgements

880 This study is partly funded by Nagra within the SANDS project. Angela Landgraf, Jens Becker (both Nagra) and Nathan Looser (ETH Zürich) are thanked for fruitful discussions. Jens Becker (Nagra) is thanked for providing us with VR data of the borehole. Laura Ziegler (RWTH Aachen) is thanked for discussions of VR data.

11 References

Anfinson, O. A., Stockli, D. F., Miller, J. C., Möller, A., and Schlunegger, F.: Tectonic Exhumation of the Central Alps
Recorded by Detrital Zircon in the Molasse Basin, Switzerland, Solid Earth, 11, 2197-2220, doi:10.5194/se-11-2197-20202020.

Ault, K. A. and Flowers, R. M.: Is apatite U–Th zonation information necessary for accurate interpretation of apatite (U–Th)/He thermochronometry data?, Geochimica et Cosmochimica Acta, 79, 60-78, doi:10.1016/j.gca.2011.11.037, 2012.

Baran, R., Friedrich, A. M., and Schlunegger, F.: The late Miocene to Holocene erosion pattern of the Alpine foreland basin
reflects Eurasian slab unloading beneath the western Alps rather than global climate change, Lithosphere, 6, 124–131,
doi:10.1130/L307.1, 2014.

Beaumont, C. and Bout, R.: Isomerization and Aromatization of Hydrocarbons and the Paleothermometry and Burial History
of Alberta Foreland Basin, AAPG Bulletin, 69(4), 546-566, doi:10.1306/AD46252E-16F7-11D7-8645000102C1865D, 1985.

Becker, A.: The Jura Mountains — an active foreland fold-and-thrust belt?, Tectonophysics, 321, 381–406,
doi:10.1016/S0040-1951(00)00089-5, 2000.

Berger, J.-P., Reichenbacher, B., Becker, D., Grimm, M., Grimm, K., Picot, L., Storni, A., Pirkenseer, C., and Schaefer, A.:
Eocene-Pliocene time scale and stratigraphy of the Upper Rhine Graben (URG) and the Swiss Molasse Basin (SMB), Int J
Earth Sci (Geol Rundsch), 94, 711–731, doi:10.1007/s00531-005-0479-y, 2005a.

Berger, J.-P., Reichenbacher, B., Becker, D., Grimm, M., Grimm, K., Picot, L., Storni, A., Pirkenseer, C., Derer, C., and
Schaefer, A.: Paleogeography of the Upper Rhine Graben (URG) and the Swiss Molasse Basin (SMB) from Eocene to
Pliocene, Int J Earth Sci (Geol Rundsch), 94, 697–710, doi:10.1007/s00531-005-0475-2, 2005b.

Bernet, M. and Spiegel, C. (Eds.): Detrital thermochronology - Provenance analysis, exhumation, and landscape evolution of
mountain belts, Geological Society of America, 2004.

Bernet, M., Zattin, M., Garver, J. I., Brandon, M. T., and Vance, J. A.: Steady-state exhumation of the European Alps, Geol.,
29, 35-38, doi:10.1130/0091-7613(2001)029<0035:SSEOTE>2.0.CO;2, 2001.

Bernet, M., Brandon, M., Garver, J., Balestieri, M. L., Ventura, B., and Zattin, M.: Exhuming the Alps through time: clues
from detrital zircon fission-track thermochronology, Basin Res., 21, 781–798, doi:10.1111/j.1365-2117.2009.00400.x, 2009.

Beydoun, Z. R., Hughes Clarke, M. W., and Stoneley, R.: Petroleum in the Zagros Basin: A Late Tertiary Foreland Basin
Overprinted onto the Outer Edge of a Vast Hydrocarbon-Rich Paleozoic-Mesozoic Passive-Margin Shelf: Chapter 11,
AAPG Special Volumes, 309–339, 1992.

Bolliger, T.: Trace fossils and trackways in the Upper Freshwater Molasse of Central and Eastern Switzerland, NJGPA, 214,
519–536, doi:10.1127/njgpa/214/1999/519, 1999.

Bourgeois, O., Ford, M., Diraison, M., Le Veslud, C. C. de, Gerbault, M., Pik, R., Ruby, N., and Bonnet, S.: Separation of
rifting and lithospheric folding signatures in the NW-Alpine foreland, Int J Earth Sci (Geol Rundsch), 96, 1003–1031,
doi:10.1007/s00531-007-0202-2, 2007.

Bousquet, R., Oberhänsli, R., Goffé, B., Wiederkehr, M., Koller, F., Schmid, S. M., Schuster, R., Engi, M., Berger, A., and Martinotti, G.: Metamorphism of metasediments at the scale of an orogen: a key to the Tertiary geodynamic evolution of the Alps, Geological Society, London, Special Publications, 298, 393–411, doi:10.1144/SP298.18, 2008.

Braun, J., van der Beek, P., Valla, P., Robert, X., Herman, F., Glotzbach, C., Pedersen, V., Perry, C., Simon-Labric, T., and
920 Prigent, C.: Quantifying rates of landscape evolution and tectonic processes by thermochronology and numerical modeling of crustal heat transport using PECUBE, Tectonophysics, 524, 1–28, doi:10.1016/j.tecto.2011.12.035, 2012.

Braun, J., Guillocheau, F., Robin, C., Baby, G., and Jelsma, H.: Rapid erosion of the Southern African Plateau as it climbs over a mantle superswell, JGR Solid Earth, 119(7), 6093-6112, doi:10.1002/2014JB010998, 2014.

Brewer, I. D., Burbank, D. W., and Hodges, K. V.: Modelling detrital cooling-age populations: insights from two Himalayan
925 catchments, Basin Research, 15, 305–320, doi:10.1046/j.1365-2117.2003.00211.x, 2003.

Brown, R. W., Beucher, R., Roper, S., Persano, C., Stuart, F., and Fitzgerald, P.: Natural age dispersion arising from the analysis of broken crystals. Part I: Theoretical basis and implications for the apatite (U–Th)/He thermochronometer, Geochimica et Cosmochimica Acta, 122, 478–497, doi:10.1016/j.gca.2013.05.041, 2013.

Buechi, M. W., Graf, H. R., Haldimann, P., Lowick, S. E., and Anselmetti, F. S.: Multiple Quaternary erosion and infill
930 cycles in overdeepened basins of the northern Alpine foreland, Swiss j geosci, 111, 133–167, doi:10.1007/s00015-017-0289-9, 2018.

Burkhard, M. and Sommaruga, A.: Evolution of the western Swiss Molasse basin: structural relations with the Alps and the Jura belt, Geological Society, London, Special Publications, 134, 279–298, doi:10.1144/GSL.SP.1998.134.01.13, 1998.

Cardello, G. L., Di Vincenzo, G., Giorgetti, G., Zwingmann, H., and Mancktelow, N.: Initiation and development of the
935 Pennine Basal Thrust (Swiss Alps): a structural and geochronological study of an exhumed megathrust, Journal of Structural Geology, 126, 338–356, doi:10.1016/j.jsg.2019.06.014, 2019.

Cecil, R. M., Saleeby, Z., Saleeby, J., and Farley, K. A.: Pliocene–Quaternary subsidence and exhumation of the southeastern San Joaquin Basin, California, in response to mantle lithosphere removal, Geosphere, 10, 129–147, doi:10.1130/GES00882.1, 2014.

940 Cederbom, C. E., Sinclair, H. D., Schlunegger, F., and Rahn, M. K.: Climate-induced rebound and exhumation of the European Alps, Geol, 32, 709, doi:10.1130/G20491.1, 2004.

Cederbom, C. E., van der Beek, P., Schlunegger, F., Sinclair, H. D., and Oncken, O.: Rapid extensive erosion of the North Alpine foreland basin at 5-4 Ma, Basin Research, 23, 528–550, doi:10.1111/j.1365-2117.2011.00501.x, 2011.

Champagnac, J.-D., Schlunegger, F., Norton, K., Blanckenburg, F. von, Abbühl, L. M., and Schwab, M.: Erosion-driven
945 uplift of the modern Central Alps, Tectonophysics, 474, 236–249, doi:10.1016/j.tecto.2009.02.024, 2009.

Crampton, S. L. and Allen, P. A.: Recognition of Forebulge Unconformities Associated with Early Stage Foreland Basin Development: Example from the North Alpine Foreland Basin, AAPG Bulletin, 79(19), 1495-1514, doi:10.1306/7834DA1C-1721-11D7-8645000102C1865D, 1995.

Davies, J. H. and von Blanckenburg, F.: Slab breakoff: A model of lithosphere detachment and its test in the magmatism and

950   deformation of collisional orogens, Earth and Planetary Science Letters, 129, 85–102, doi:10.1016/0012-821X(94)00237-S,

1995.

Deming, D., Sass, J. H., Lachenbruch, A. H., and de Rito, R. F.: Heat flow and subsurface temperature as evidence for basin-

scale ground-water flow, North Slope of Alaska, Geological Society of America Bulletin, 104(5), 528-542,

doi:10.1130/0016-7606(1992)104<0528:HFASTA>2.3.CO;2, 1992.

955   Diebold, P.: Der Nordschweizer Permokarbon-Trog und die Steinkohlenfrage der Nordschweiz., Beiträge zur Geologie der

Schweiz, Kleinere Mitteilungen, 81, 143–174, 1989.

Diebold, P. and Noack, T.: Late Paleozoic troughs and Tertiary structures in the eastern folded Jura, in: Deep structure of the

Swiss Alps: results of NRP 20, edited by: Pfiffner, O. A., Lehner, P., Heitzmann, P., St. Mueller, and Steck, A., Birkhäuser

Verlag, Basel, Switzerland, 59–63, 1997.

960   Diebold, P., Naef, H., and Ammann, M.: Zur Tektonik der zentralen Nordschweiz, Nagra Technischer Bericht, NTB 90-04,

1991.

Djimbi, D. M., Gautheron, C., Roques, J., Tassan-Got, L., Gerin, C., and Simoni, E.: Impact of apatite chemical composition

on (U-Th)/He thermochronometry: An atomistic point of view, Geochimica et Cosmochimica Acta, 167, 162-176,

doi:10.1016/j.gca.2015.06.017, 2015.

965   Echtler, H. P. and Chauvet, A.: Carboniferous convergence and subsequent crustal extension in the southern Schwarzwald

(SW Germany), Geodinamica Acta, 5, 37–49, doi:10.1080/09853111.1992.11105218, 1992.

Egli, D., Mancktelow, N., and Spikings, R.: Constraints from 40 Ar/ 39 Ar geochronology on the timing of Alpine shear

zones in the Mont Blanc-Aiguilles Rouges region of the European Alps, Tectonics, 36, 730–748,

doi:10.1002/2016TC004450, 2017a.

970   Egli, D., Mosar, J., Ibele, T., and Madritsch, H.: The role of precursory structures on Tertiary deformation in the Black

Forest—Hegau region, Int J Earth Sci (Geol Rundsch), 106, 2297–2318, doi:10.1007/s00531-016-1427-8, 2017b.

Ehlers, T. A. and Farley, K. A.: Apatite (U–Th)/He thermochronometry: methods and applications to problems in tectonic

and surface processes, Earth and Planetary Science Letters, 206, 1–14, doi:10.1016/S0012-821X(02)01069-5, 2003.

Eisbacher, G. H., Lüschen, E., and Wickert, F.: Crustal-scale thrusting and extension in the Hercynian Schwarzwald and

975   Vosges, central Europe, Tectonics, 8, 1–21, doi:10.1029/TC008i001p00001, 1989.

Farley, K. A.: Helium diffusion from apatite: General behavior as illustrated by Durango fluorapatite, JGR: Solid Earth,

105(B2), 2903–2914, doi: 10;105(B2):2903-14, 2000.

Fillon, C., Gautheron, C., and van der Beek, P.: Oligocene–Miocene burial and exhumation of the Southern Pyrenean

foreland quantified by low-temperature thermochronology, Journal of the Geological Society, 170, 67–77,

980   doi:10.1144/jgs2012-051, 2013.

Fitzgerald, P. G., Baldwin, S. L., Webb, L. E., and O'Sullivan, P.: Interpretation of (U–Th)/He single grain ages from slowly cooled crustal terranes: A case study from the Transantarctic Mountains of southern Victoria Land, Chemical Geology, 225, 91–120, doi:10.1016/j.chemgeo.2005.09.001, 2006.

Fitzgerald, P. G., Duebendorfer, E. M., Faulds, J. E., and O'Sullivan, P.: South Virgin-White Hills detachment fault system of SE Nevada and NW Arizona: Applying apatite fission track thermochronology to constrain the tectonic evolution of a major continental detachment fault, Tectonics, 28, TC2001, doi:10.1029/2007TC002194, 2009.

Flowers, R. M.: Exploiting radiation damage control on apatite (U–Th)/He dates in cratonic regions, Earth and Planetary Science Letters, 277, 148–155, doi:10.1016/j.epsl.2008.10.005, 2009.

Flowers, R. M., Ketcham, R. A., Macdonald, F. A., Siddoway, C. S., and Havranek, R. E.: Existing thermochronologic data do not constrain Snowball glacial erosion below the Great Unconformities. Proceedings of the National Academy of Sciences, 119(38), e2208451119, 2022.

Folguera, A., Bottesi, G., Duddy, I., Martín-González, F., Orts, D., Sagripanti, L., Rojas Vera, E., and Ramos, V.A.: Exhumation of the Neuquén Basin in the southern Central Andes (Malargüe fold and thrust belt) from field data and low-temperature thermochronology, Journal of South American Earth Science, 64, 381-398, doi:10.1016/j.jsames.2015.08.003, 2015.

Fox, M. and Shuster, D. L.: The influence of burial heating on the (U–Th)/He system in apatite: Grand Canyon case study, Earth and Planetary Science Letters, 397, 174–183, doi:10.1016/j.epsl.2014.04.041, 2014.

Fox, M., Dai, J.-G., and Carter, A.: Badly Behaved Detrital (U-Th)/He Ages: Problems With He Diffusion Models or Geological Models?, Geochem. Geophys. Geosyst., 20(5), 2418-2432, doi:10.1029/2018GC008102, 2019.

François, T., Agard, P., Bernet, M., Meyer, B., Chung, S.-L., Zarrinkoub, M. H., Burov, E., and Monié, P.: Cenozoic exhumation of the internal Zagros: first constraints from low-temperature thermochronology and implications for the build-up of the Iranian plateau, Lithos, 206-207, 100–112, doi:10.1016/j.lithos.2014.07.021, 2014.

Fry, B., Deschamps, F., Kissling, E., Stehly, L., and Giardini, D.: Layered azimuthal anisotropy of Rayleigh wave phase velocities in the European Alpine lithosphere inferred from ambient noise, Earth and Planetary Science Letters, 297, 95–102, doi:10.1016/j.epsl.2010.06.008, 2010.

Gallagher, K.: Transdimensional inverse thermal history modeling for quantitative thermochronology, J. Geophys. Res., 117, B02408, doi:10.1029/2011JB008825, 2012.

Gallagher, K. and Ketcham, R. A.: Comment on "Thermal history modelling: HeFTy vs. QTQt" by Vermeesch and Tian, Earth-Science Reviews (2014), 139, 279–290, Earth-Science Reviews, 176, 387–394, doi:10.1016/j.earscirev.2017.11.001, 2018.

Ganti, V., von Hagke, C., Scherler, D., Lamb, M. P., Fischer, W. W., and Avouac, J.-P.: Time scale bias in erosion rates of glaciated landscapes, Science Advances, 2, e1600204, doi:10.1126/sciadv.1600204, 2016.

Genser, J., Cloetingh, S. A., and Neubauer, F.: Late orogenic rebound and oblique Alpine convergence: New constraints from subsidence analysis of the Austrian Molasse basin, Global and Planetary Change, 58, 214–223, doi:10.1016/j.gloplacha.2007.03.010, 2007.

Geyer, O. F., Gwinner, M. P., Geyer, M., Nitsch, E., and Simon, T.: Geologie von Baden-Württemberg: Mit 4 Tabellen, 5., völlig neu bearb. Aufl., Schweizerbart, Stuttgart, X, 627 S, 2011.

Giamboni, M., Ustaszewski, K., Schmid, S. M., Schumacher, M. E., and Wetzel, A.: Plio-Pleistocene transpressional reactivation of Paleozoic and Paleogene structures in the Rhine-Bresse transform zone (northern Switzerland and eastern France), Int J Earth Sci (Geol Rundsch), 93, 207–223, doi:10.1007/s00531-003-0375-2, 2004.

Glotzbach, C., van der Beek, P. A., and Spiegel, C.: Episodic exhumation and relief growth in the Mont Blanc massif, Western Alps from numerical modelling of thermochronology data, Earth and Planetary Science Letters, 304, 417–430, doi:10.1016/j.epsl.2011.02.020, 2011a.

Glotzbach, C., Bernet, M., and van der Beek, P.: Detrital thermochronology records changing source areas and steady exhumation in the Western European Alps, Geol, 39, 239–242, doi:10.1130/G31757.1, 2011b.

Green, P. and Duddy, I.: Apatite (U-Th-Sm)/He thermochronology on the wrong side of the tracks, Chemical Geology, 488, 21–33, doi:10.1016/j.chemgeo.2018.04.028, 2018.

Griesser, J.-C. and Rybach, L.: Numerical Thermohydraulic Modeling of Deep Groundwater Circulation in Crystalline Basement: An Example of Calibration, in: Hydrogeological Regimes and Their Subsurface Thermal Effects, edited by: Beck, A. E., Garven, G., and Stegena, L., American Geophysical Union, Washington, D. C., 65–74, doi:10.1029/GM047p0065, 1989.

Güldenpfennig, M. and Loeschke, J.: Petrographie und Geochemie unterkarbonischer Grauwacken und Vulkanite der Zone von Badenweiler-Lenzkirch und der Umgebung von Präg, Jahreshefte des Geologischen Landesamts Baden-Würtemberg, 33, 5–32, 1991.

Gusterhuber, J., Hinsch, R., and Sachsenhofer, R. F.: Evaluation of hydrocarbon generation and migration in the Molasse fold and thrust belt(Central Eastern Alps, Austria) using structural and thermal basin models, AAPG Bulletin, 98, 253–277, doi:10.1306/06061312206, 2014.

Haldimann, P., Graf, H. R., and Jost, J.: Geologischer Atlas der Schweiz, 1071 Bülach, Erläuterungen, Bundesamt für Landestopographie Swisstopo, 2017.

Handy, M. R., M. Schmid, S., Bousquet, R., Kissling, E., and Bernoulli, D.: Reconciling plate-tectonic reconstructions of Alpine Tethys with the geological–geophysical record of spreading and subduction in the Alps, Earth-Science Reviews, 102, 121–158, doi:10.1016/j.earscirev.2010.06.002, 2010.

Herman, F., Seward, D., Valla, P. G., Carter, A., Kohn, B., Willett, S. D., and Ehlers, T. A.: Worldwide acceleration of mountain erosion under a cooling climate, Nature, 504, 423–426, doi:10.1038/nature12877., 2013.

Herwegh, M., Berger, A., Baumberger, R., Wehrens, P., and Kissling, E.: Large-Scale Crustal-Block-Extrusion During Late Alpine Collision, Scientific reports, 7(1), 1-10, doi:10.1038/s41598-017-00440-0, 2017.

Herwegh, M., Berger, A., Glotzbach, C., Wangenheim, C., Mock, S., Wehrens, P., Baumberger, R., Egli, D., and Kissling, E.: Late stages of continent-continent collision: Timing, kinematic evolution, and exhumation of the Northern rim (Aar Massif) of the Alps, Earth-Science Reviews, 200, 102959, doi:10.1016/j.earscirev.2019.102959, 2020.

1050 Hinsch, R.: Laterally varying structure and kinematics of the Molasse fold and thrust belt of the Central Eastern Alps: Implications for exploration, AAPG Bulletin, 97, 1805–1831, doi:10.1306/04081312129, 2013.

Hinsken, S., Ustaszewski, K., and Wetzel, A.: Graben width controlling syn-rift sedimentation: the Palaeogene southern Upper Rhine Graben as an example, Int J Earth Sci (Geol Rundsch), 96, 979–1002, doi:10.1007/s00531-006-0162-y, 2007.

Hofmann, F.: Vulkanische Tuffe auf dem Wellenberg E von Frauenfeld und neue Funde auf dem thurgauischen Seerücken, 1055 1975.

Hurford, A. J.: Cooling and uplift patterns in the Lepontine Alps South Central Switzerland and an age of vertical movement on the Insubric fault line, Contrib Mineral and Petrol, 92, 413–427, doi:10.1007/BF00374424, 1986.

Jordan, P.: Evidence for large-scale decoupling in Triassic evaporites of northern Switzerland: an overview, Eclogae geol. Helv., 85(3), 677–693, 1992.

1060 Jordan, P., Malz, A., Heuberger, S., Pietsch, J., Kley, J., and Madritsch, H.: Regionale geologische Profilschnitte durch die Nordschweiz und 2DBilanzierung der Fernschubdeformation im östlichen Faltenjura: Arbeitsbericht zu SGT Etappe 2, Nagra Arbeitsbericht, 2015.

Kämpfen, W.: Geologischer Atlas der Schweiz, 1972.

Kempf, O., Bollinger, T., Kälin, D., Engesser, B., and Matter, A.: New magnetostratigraphic calibration of Early to Middle 1065 Miocene mammal biozones of the North Alpine foreland basin, in: Actes du Congrès BiochroM'97, edited by: Aguilar, J.-P., Legendre, S., and Michaux, J., Montpellier, 547–561, 1997.

Kempf, O., Matter, A., Burbank, D. W., and Mange, M.: Depositional and structural evolution of a foreland basin margin in a magnetostratigraphic framework: the eastern Swiss Molasse Basin, Int J Earth Sci (Geol Rundsch), 88, 253–275, doi:10.1007/s005310050263, 1999.

1070 Ketcham, R. A.: Forward and Inverse Modeling of Low-Temperature Thermochronometry Data, Reviews in Mineralogy and Geochemistry, 58, 275–314, doi:10.2138/rmg.2005.58.11, 2005.

Kissling, E. and Schlunegger, F.: Rollback Orogeny Model for the Evolution of the Swiss Alps, Tectonics, 37, 1097–1115, doi:10.1002/2017TC004762, 2018.

Koshnaw, R. I., Horton, B. K., Stockli, D. F., Barber, D. E., Tamar-Agha, M. Y., and Kendall, J. J.: Neogene shortening and 1075 exhumation of the Zagros fold-thrust belt and foreland basin in the Kurdistan region of northern Iraq, Tectonophysics, 694, 332–355, doi:10.1016/j.tecto.2016.11.016, 2017.

Kuhlemann, J. and Kempf, O.: Post-Eocene evolution of the North Alpine Foreland Basin and its response to Alpine tectonics, Sedimentary Geology, 152(1-2), 45–78, doi:10.1016/S0037-0738(01)00285-8, 2002.

Kuhlemann, J. and Rahn, M.: Plio-Pleistocene landscape evolution in Northern Switzerland, Swiss j geosci, 106, 451–467, 1080 doi:10.1007/s00015-013-0152-6, 2013.

Lacombe, O., Mazzoli, S., Hagke, C. von, Rosenau, M., Fillon, C., and Granado, P.: Style of deformation and tectono-sedimentary evolution of fold-and-thrust belts and foreland basins: From nature to models, Tectonophysics, 767, 228163, doi:10.1016/j.tecto.2019.228163, 2019.

Laubscher, H. P.: Foreland folding, Tectonophysics, 47, 325–337, doi:10.1016/0040-1951(78)90037-9, 1978.

1085   Laubscher, H. P.: The eastern Jura: Relations between thin-skinned and basement tectonics, local and regional, Geol. Runsch., 75, 536-553, 1986.

Levina, M., Horton, B. K., Fuentes, F., and Stockli, D. F.: Cenozoic sedimentation and exhumation of the foreland basin system preserved in the Precordillera thrust belt (31-32°S), southern central Andes, Argentina, Tectonics, 33, 1659–1680, doi:10.1002/2013TC003424, 2014.

1090   Lippitsch, R.: Upper mantle structure beneath the Alpine orogen from high-resolution teleseismic tomography, J. Geophys. Res., 108(B8), doi:10.1029/2002JB002016, 2003.

Littke, R., Büker, C., Hertle, M., Karg, H., Stroetmann-Heinen, V., and Oncken, O.: Heat flow evolution, subsidence and erosion in the Rheno-Hercynian orogenic wedge of central Europe, Geological Society, London, Special Publications, 179, 231–255, doi:10.1144/GSL.SP.2000.179.01.15, 2000.

1095   Looser, N., Madritsch, H., Guillong, M., Laurent, O., Wohlwend, S., and Bernasconi, S. M.: Absolute Age and Temperature Constraints on Deformation Along the Basal Décollement of the Jura Fold-and-Thrust Belt From Carbonate U-Pb Dating and Clumped Isotopes, Tectonics, 40, e2020TC006439, doi:10.1029/2020TC006439, 2021.

Louis, S., Luijendijk, E., Dunkl, I., and Person, M.: Episodic fluid flow in an active fault, Geol, 47, 938–942, doi:10.1130/G46254.1, 2019.

1100   Lucas, J. and Prevot-Lucas, L.: On the Genesis of Sedimentary Apatite and Phosphate-Rich Sediments, in: Soils and Sediments, edited by: Paquet, H. and Clauer, N., Springer Berlin Heidelberg, Berlin, Heidelberg, 249–268, doi:10.1007/978-3-642-60525-3_12, 1997.

Luijendijk, E.: Beo v1.0: numerical model of heat flow and low-temperature thermochronology in hydrothermal systems, Geosci. Model Dev., 12, 4061–4073, doi:10.5194/gmd-12-4061-2019, 2019.

1105   Luijendijk, E., van Balen, R. T., Voorde, M. ter, and Andriessen, P. A. M.: Reconstructing the Late Cretaceous inversion of the Roer Valley Graben (southern Netherlands) using a new model that integrates burial and provenance history with fission track thermochronology, J. Geophys. Res., 116(B6), doi:10.1029/2010JB008071, 2011.

Lyon-Caen, H. and Molnar, P.: Constraints on the deep structure and dynamic processes beneath the Alps and adjacent regions from an analysis of gravity anomalies, Geophysical Journal International, 99, 19–32, doi:10.1111/j.1365-

1110   246X.1989.tb02013.x, 1989.

Madritsch, H., Naef, H., Meier, B., Franzke, H. J., and Schreurs, G.: Architecture and Kinematics of the Constance-Frick Trough (Northern Switzerland): Implications for the Formation of Post-Variscan Basins in the Foreland of the Alps and Scenarios of Their Neogene Reactivation, Tectonics, 37, 2197–2220, doi:10.1029/2017TC004945, 2018.

Malusà, M. G., Polino, R., Zattin, M., Bigazzi, G., Martin, S., and Piana, F.: Miocene to Present differential exhumation in

1115   the Western Alps: Insights from fission track thermochronology, Tectonics, 24, TC3004, doi:10.1029/2004TC001782, 2005.

Malz, A., Madritsch, H., Meier, B., and Kley, J.: An unusual triangle zone in the external northern Alpine foreland (Switzerland): Structural inheritance, kinematics and implications for the development of the adjacent Jura fold-and-thrust belt, Tectonophysics, 670, 127–143, doi:10.1016/j.tecto.2015.12.025, 2016.

Marchant, R., Ringgenberg, Y., Stampfli, G., Birkhäuser, P., Roth, P., and Meier, B.: Paleotectonic evolution of the Zürcher

1120   Weinland (northern Switzerland), based on 2D and 3D seismic data, Eclogae geol. Helv., 98, 345–362, doi:10.1007/s00015-005-1171-8, 2005.

Matter, A., Homewood, P., Caron, C., Rigassi, D., van Stujivenberg, J., Weidmann, M., and Winkler, W.: Flysch and molasse of western and central Switzerland, in: Geology of Switzerland, A Guidebook, Part B, Excursions, edited by: Trümpy, R., Schweiz. Geol. Komm., Wepf, Basel, Switzerland, 261–293, 1980.

1125   Mazurek, M.: Phase equilibria and oxygen isotopes in the evolution of metapelitic migmatites: a case study from the Pre-Alpine basement of Northern Switzerland, Contrib Mineral and Petrol, 109, 494–510, doi:10.1007/BF00306552, 1992.

Mazurek, M.: Geology of the crystalline basement of Northern Switzerland and derivation of geological input data for safety assessment models, Nagra technical Report NTB 93-12, Wettingen, Switzerland, 1998.

Mazurek, M., Hurford, A. J., and Leu, W.: Unravelling the multi-stage burial history of the Swiss Molasse Basin: integration

1130   of apatite fission track, vitrinite reflectance and biomarker isomerisation analysis, Basin Research, 18, 27–50, doi:10.1111/j.1365-2117.2006.00286.x, 2006.

Medici, F. and Rybach, L.: Geothermal map of Switzerland 1:500.000 (Heat Flow Density), Beitr. Geol. Schweiz, 1995.

Meyer, H., Hetzel, R., Fügenschuh, B., and Strauss, H.: Determining the growth rate of topographic relief using in situ-produced 10Be: A case study in the Black Forest, Germany, Earth and Planetary Science Letters, 290, 391–402,

1135   doi:10.1016/j.epsl.2009.12.034, 2010.

Mock, S., Hagke, C. von, Schlunegger, F., Dunkl, I., and Herwegh, M.: Long-wavelength late-Miocene thrusting in the north Alpine foreland: implications for late orogenic processes, Solid Earth, 11, 1823–1847, doi:10.5194/se-11-1823-2020, 2020.

Moeck, I., Block, T., Graf, R., Heuberger, S., Kuhn, P., Naef, H., Sonderegger, M., Uhlig, S., and Wolfgramm, M.: The St. Gallen Project: Development of Fault Controlled Geothermal Systems in Urban Areas, Proceedings World Geothermal

1140   Congress, 2015.

Molnar, P, and England, P.: Late Cenozoic uplift of mountain ranges and global climate change: chicken or egg?, Nature, 346(6279, 29-34, 1990.

Mosar, J., Stampfli, G. M., and Francois, G.: Western Préalpes Médianes Romandes: Timing and structure. A review, Eclogae geol. Helv., 89, 389–425, 1996.

1145   Mosar, J.: Present-day and future tectonic underplating in the western Swiss Alps: reconciliation of basement/wrench-faulting and décollement folding of the Jura and Molasse basin in the Alpine foreland, Earth and Planetary Science Letters, 173, 143–155, doi:10.1016/S0012-821X(99)00238-1, 1999.

Mosbrugger, V., Utescher, T., and Dilcher, D. L.: Cenozoic continental climatic evolution of Central Europe, PNAS, 102(42), 14964–14969, doi:10.1073/pnas.0505267102, 2005.

1150 Nagra: SGT Etappe 2: Vorschlag weiter zu untersuchender geologischer Standortgebiete mit zugehörigen Standortarealen für die Oberflächenanlage. Geologische Grundlagen. Dossier II: Sedimentologische und tektonische Verhältnisse., Nagra Tech. Ber., Wettingen, 2014.

Nagra: Preliminary horizon and structure mapping of the 3D-seismic NL-16 in time domain. Nagra Project Report NAB 18-35, Wettingen, 2019.

1155 Nagra: TBO Bülach-1-1: Data Report (Dossier I-X), 2020.

Omodeo-Salé, S., Hamidi, Y., Villagomez, D., and Moscariello, A.: Quantifying Multiple Erosion Events in the Distal Sector of the Northern Alpine Foreland Basin (North-Eastern Switzerland), by Combining Basin Thermal Modelling with Vitrinite Reflectance and Apatite Fission Track Data, Geosciences, 11, 62, doi:10.3390/geosciences11020062, 2021.

Ortner, H., Aichholzer, S., Zerlauth, M., Pilser, R., and Fügenschuh, B.: Geometry, amount, and sequence of thrusting in the

1160 Subalpine Molasse of western Austria and southern Germany, European Alps, Tectonics, 34, 1–30, doi:10.1002/2014TC003550, 2015.

Ortner, H., von Hagke, C., Sommaruga, A.,Mock, S., Mosar, J., Hinsch, R., Beidinger, A.: The northern Deformation Front of the European Alps. In Bellahsen, N. & Rosenberg C. (eds.) The Alpine Chain, ISTE-Wiley editions, 2021.

Persaud, M. and Pfiffner, O.: Active deformation in the eastern Swiss Alps: post-glacial faults, seismicity and surface uplift,

1165 Tectonophysics, 385, 59–84, doi:10.1016/j.tecto.2004.04.020, 2004.

Pfiffner, O. A.: Evolution of the North Alpine Foreland Basin in the Central Alps, in: Foreland Basins, edited by: Allen, P. A. and Homewood, P., Blackwell Publishing Ltd, Oxford, UK, 219–228, doi:10.1002/9781444303810.ch11, 1986.

Pfiffner, O. A.: Structural Map of the Helvetic Zone of the Swiss Alps, including Vorarlberg (Austria) and Haute Savoie (France), Federal Office of Topography swisstopo, 2011.

1170 Pfiffner, O. A., Schlunegger, F., and Buiter, S. J. H.: The Swiss Alps and their peripheral foreland basin: Stratigraphic response to deep crustal processes, Tectonics, 21(2), 3-1, doi:10.1029/2000TC900039, 2002.

Pola, M., Cacace, M., Fabbri, P., Piccinini, L., Zampieri, D., and Torresan, F.: Fault Control on a Thermal Anomaly: Conceptual and Numerical Modeling of a Low-Temperature Geothermal System in the Southern Alps Foreland Basin (NE Italy), J. Geophys. Res. Solid Earth, 125(5), e2019JB017394, doi:10.1029/2019JB017394, 2020.

1175 Pollhammer, T., Salcher, B., Kober, F., and Deplazes, G.: GIS-based morphostratigraphic analysis of glaciofluvial terrace hypsometry in the North Alpine Foreland using R, EGU General Assembly 2022, Vienna, Austria, 23–27 May 2022, EGU22-7472, doi:10.5194/egusphere-egu22-7472, 2022.

Rahn, M. K. and Selbekk, R.: Absolute dating of the youngest sediments of the Swiss Molasse basin by apatite fission track analysis, Swiss j geosci, 100, 371–381, doi:10.1007/s00015-007-1234-0, 2007.

1180   Reinecker, J., Danišík, M., Schmid, C., Glotzbach, C., Rahn, M., Frisch, W., and Spiegel, C.: Tectonic control on the late stage exhumation of the Aar Massif (Switzerland): Constraints from apatite fission track and (U-Th)/He data, Tectonics, 27, TC6009, doi:10.1029/2007TC002247, 2008.

Reiners, P. W. and Brandon, M. T.: Using thermochronology to understand orogenic erosion, Annu. Rev. Earth Planet. Sci., 34, 419–466, doi:10.1146/annurev.earth.34.031405.125202, 2006.

1185   Robl, J., Hergarten, S., and Prasicek, G.: The topographic state of fluvially conditioned mountain ranges, Earth-Science Reviews, 168, 190-217, doi:10.1016/j.earscirev.2017.03.007, 2017.

Roche, V., Childs, C., Madritsch, H., and Camanni, G.: Layering and structural inheritance controls on fault zone structure in three dimensions: a case study from the northern Molasse Basin, Switzerland, Journal of the Geological Society, 177, 493–508, doi:10.1144/jgs2019-052, 2020.

1190   Sawatzki, G. and Hann, H. P.: Badenweiler-Lenzkirch-Zone (Südschwarzwald). Geologische Karte von Baden-Württemberg, 2003.

Schaltegger, U.: U-Pb geochronology of the Southern Black Forest Batholith (Central Variscan Belt): timing of exhumation and granite emplacement, Int J Earth Sci (Geol Rundsch), 88, 814–828, doi:10.1007/s005310050308, 2000.

Schegg, R. and Leu, W.: Analysis of erosion events and palaeogeothermal gradients in the North Alpine Foreland Basin of
1195   Switzerland, Geological Society, London, Special Publications, 141, 137–155, doi:10.1144/GSL.SP.1998.141.01.09, 1998.

Schildgen, T. F., van der Beek, P. A., Sinclair, H. D., and Thiede, R. C.: Spatial correlation bias in late-Cenozoic erosion histories derived from thermochronology, Nature, 559, 89–93, doi:10.1038/s41586-018-0260-6, 2018.

Schlunegger, F. and Mosar, J.: The last erosional stage of the Molasse Basin and the Alps, Int J Earth Sci (Geol Rundsch), 100, 1147–1162, doi:10.1007/s00531-010-0607-1, 2011.

1200   Schlunegger, F. and Kissling, E.: Slab rollback orogeny in the Alps and evolution of the Swiss Molasse basin, Nature communications, 6(1), 1-10, doi:10.1038/ncomms9605, 2015.

Schlunegger, F. and Castelltort, S.: Immediate and delayed signal of slab breakoff in Oligo/Miocene Molasse deposits from the European Alps, Scientific reports, 6(1), 1-11, doi:10.1038/srep31010, 2016.

Schlunegger, F., Matter, A., Burbank, D. W., and Klaper, E. M.: Magnetostratigraphic constraints on relationships between
1205   evolution of the central Swiss Molasse basin and Alpine orogenic events, Geological Society of America Bulletin, 109, 225–241, doi:10.1130/0016-7606(1997)109<0225:MCORBE>2.3.CO;2, 1997.

Schlunegger, F., Rieke-Zapp, D., and Ramseyer, K.: Possible environmental effects on the evolution of the Alps-Molasse Basin system, Swiss j geosci, 100, 383–405, doi:10.1007/s00015-007-1238-9, 2007.

Schmid, S. M., Pfiffner, O. A., Froitzheim, N., Schönborn, G., and Kissling, E.: Geophysical-geological transect and tectonic
1210   evolution of the Swiss-Italian Alps, Tectonics, 15, 1036–1064, doi:10.1029/96tc00433, 1996.

Schmid, S. M., Fgenschuh, B., Kissling, E., and Schuster, R.: Tectonic map and overall architecture of the Alpine orogen, Eclogae geol. Helv., 97, 93–117, doi:10.1007/s00015-004-1113-x, 2004.

Schreiner, A.: Erläuterungen zu Blatt Hegau und westlicher Bodensee, Geologisches Landesamt Baden-Würtemberg, Freiburg, Stuttgart, 290pp, 1992.

1215 Shuster, D. L., Flowers, R. M., and Farley, K. A.: The influence of natural radiation damage on helium diffusion kinetics in apatite, Earth and Planetary Science Letters, 249, 148–161, doi:10.1016/j.epsl.2006.07.028, 2006.

Sinclair, H. D.: Flysch to molasse transition in peripheral foreland basins: The role of the passive margin versus slab breakoff, Geol, 25(12), 1123-1126, doi:10.1130/0091-7613(1997)025<1123:FTMTIP>2.3.CO;2, 1997.

Sinclair, H. D. and Allen, P. A.: Vertical versus horizontal motions in the Alpine orogenic wedge: stratigraphic response in

1220 the foreland basin, Basin Research, 4, 215–232, doi:10.1111/j.1365-2117.1992.tb00046.x, 1992.

Sinclair, H. D., Coakley, B. J., Allen, P. A., and Watts, A. B.: Simulation of Foreland Basin Stratigraphy using a diffusion model of mountain belt uplift and erosion: An example from the central Alps, Switzerland, Tectonics, 10, 599–620, doi:10.1029/90TC02507, 1991.

Sommaruga, A., Burkhard, M., Laubscher, H., Noack, T., and Diebold, P.: Jura Mountains, in: Deep structure of teh Swiss

1225 Alps: results of NRP 20, edited by: Pfiffner, O. A., Lehner, P., Heitzmann, P., St. Mueller, and Steck, A., Birkhäuser Verlag, Basel, Switzerland, 45–63, doi:10.1007/978-3-0348-9098-4_7, 1997.

Sonney, R. and Vuataz, F.-D.: Properties of geothermal fluids in Switzerland: A new interactive database, Geothermics, 37, 496–509, doi:10.1016/j.geothermics.2008.07.001, 2008.

Spiegel, C., Kuhlemann, J., Dunkl, I., and Frisch, W.: Paleogeography and catchment evolution in a mobile orogenic belt:

1230 the Central Alps in Oligo–Miocene times, Tectonophysics, 341, 33–47, doi:10.1016/S0040-1951(01)00187-1, 2001.

Spiegel, C., Siebel, W., Kuhlemann, J., and Frisch, W.: Toward a comprehensive provenance analysis: A multi-method approach and its implications for the evolution of the Central Alps, Geological Society of America Special Paper, 37–50, 2004.

Spiegel, C., Kuhlemann, J., and Frisch, W.: Tracing sediment pathways by zircon fission track analysis: Oligocene marine

1235 connections in Central Europe, Int J Earth Sci (Geol Rundsch), 96, 363–374, doi:10.1007/s00531-006-0097-3, 2007.

Stalder, N. F., Herman, F., Fellin, M. G., Coutand, I., Aguilar, G., Reiners, P. W., and Fox, M.: The relationships between tectonics, climate and exhumation in the Central Andes (18–36°S): Evidence from low-temperature thermochronology, Earth-Science Reviews, 210, 103276, doi:10.1016/j.earscirev.2020.103276, 2020.

Stampfli, G. M. and Marchant, R. H.: Geodynamic evolution of the Tethyan margins of the Western Alps, in: Deep structure

1240 of teh Swiss Alps: results of NRP 20, edited by: Pfiffner, O. A., Lehner, P., Heitzmann, P., St. Mueller, and Steck, A., Birkhäuser Verlag, Basel, Switzerland, 223–240, 1997.

Strasser, A., Charollais, J., Conrad, M. A., Clavel, B., Pictet, A., and Mastrangelo, B.: The Cretaceous of the Swiss Jura Mountains: an improved lithostratigraphic scheme, Swiss j geosci, 109, 201–220, doi:10.1007/s00015-016-0215-6, 2016.

Tatzel, M., Dunkl, I., and Eynatten, H. von: Provenance of Palaeo-Rhine sediments from zircon thermochronology,

1245 geochemistry, U/Pb dating and heavy mineral assemblages, Basin Res, 29, 396–417, doi:10.1111/bre.12155, 2017.

Timar-Geng, Z., Fügenschuh, B., Schaltegger, U., and Wetzel, A.: The impact of the Jurassic hydrothermal activity on zircon fission track data from the southern Upper Rhine Graben area, Schweizerische Mineralogische und Petrographische Mitteilungen, 84, 257–269, 2004.

Tributh, H. and Lagaly, G.: Aufbereitung und Identifizierung von Boden-und Lagerstättentonen. I: Aufbereitung der Proben 1250   im Labor., GIT-Fachzeitschrift für das Laboratorium, 30, 524–529, 1986.

Valla, P. G., van der Beek, P. A., Shuster, D. L., Braun, J., Herman, F., Tassan-Got, L., and Gautheron, C.: Late Neogene exhumation and relief development of the Aar and Aiguilles Rouges massifs (Swiss Alps) from low-temperature thermochronology modeling and 4 He/ 3 He thermochronometry, J. Geophys. Res., 117, F01004, doi:10.1029/2011JF002043, 2012.

1255   van der Beek, P., Robert, X., Mugnier, J.-L., Bernet, M., Huyghe, P., and Labrin, E.: Late Miocene – Recent exhumation of the central Himalaya and recycling in the foreland basin assessed by apatite fission-track thermochronology of Siwalik sediments, Nepal. Basin Research, 18(4), 413-434, doi:10.1111/j.1365-2117.2006.00305.x, 2006.

Vermeesch, P. and Tian, Y.: Thermal history modelling: HeFTy vs. QTQt, Earth-Science Reviews, 139, 279–290, doi:10.1016/j.earscirev.2014.09.010, 2014.

1260   Vermeesch, P. and Tian, Y.: Reply to Comment on "Thermal history modelling: HeFTy vs. QTQt" by K. Gallagher and R.A. Ketcham, Earth-Science Reviews, 176, 395–396, doi:10.1016/j.earscirev.2017.11.015, 2018.

Villagómez Díaz, D., Omodeo-Salé, S., Ulyanov, A., and Moscariello, A.: Insights into the Thermal History of North-Eastern Switzerland—Apatite Fission Track Dating of Deep Drill Core Samples from the Swiss Jura Mountains and the Swiss Molasse Basin, Geosciences, 11(1), 10, doi:10.3390/geosciences11010010, 2021.

1265   von Eynatten, H. von, Kley, J., Dunkl, I., Hoffmann, V.-E., and Simon, A.: Late Cretaceous to Paleogene exhumation in Central Europe – localized inversion vs. large-scale domal uplift, Solid Earth, 12, 935-958, doi:10.5194/se-12-935-2021, 2021.

von Hagke, C., Cederbom, C. E., Oncken, O., Stöckli, D. F., Rahn, M. K., and Schlunegger, F.: Linking the northern Alps with their foreland: The latest exhumation history resolved by low-temperature thermochronology, Tectonics, 31, TC5010, 1270   doi:10.1029/2011TC003078, 2012.

von Hagke, C., Oncken, O., and Evseev, S.: Critical taper analysis reveals lithological control of variations in detachment strength: An analysis of the Alpine basal detachment (Swiss Alps), Geochem. Geophys. Geosyst., 15, 176–191, doi:10.1002/2013GC005018, 2014a.

von Hagke, C., Oncken, O., Ortner, H., Cederbom, C. E., and Aichholzer, S.: Late Miocene to present deformation and 1275   erosion of the Central Alps — Evidence for steady state mountain building from thermokinematic data, Tectonophysics, 632, 250–260, doi:10.1016/j.tecto.2014.06.021, 2014b.

von Hagke, C., Lujiendjik, E., Ondrak, R., and Lindow, J.: Quantifying erosion rates in the Molasse basin using a high resolution data set and a new thermal model, gr, 97, 94–97, doi:10.1127/1864-5658/2015-36, 2015.

Ward, B.: Near-surface ocean temperature, J. Geophys. Res., 111(C2), doi:10.1029/2004JC002689, 2006.

1280 Weides, S. and Majorowicz, J.: Implications of Spatial Variability in Heat Flow for Geothermal Resource Evaluation in Large Foreland Basins: The Case of the Western Canada Sedimentary Basin, Energies, 7, 2573–2594, doi:10.3390/en7042573, 2014.

Wetzel, A., Allenbach, R., and Allia, V.: Reactivated basement structures affecting the sedimentary facies in a tectonically "quiescent" epicontinental basin: an example from NW Switzerland, Sedimentary Geology, 157, 153–172,

1285 doi:10.1016/S0037-0738(02)00230-0, 2003.

Willenbring, J. K., and von Blanckenburg, F.: Long-term stability of global erosion rates and weathering during late-Cenozoic cooling, Nature, 465(7295), 211-214, doi:10.1038/nature09044, 2010.

Willett, S. D. and Schlunegger, F.: The last phase of deposition in the Swiss Molasse Basin: from foredeep to negative-alpha basin, Basin Research, 22, 623–639, doi:10.1111/j.1365-2117.2009.00435.x, 2010.

1290 Wolf, R. A., Farley, K. A., and Silver, L. T.: Helium diffusion and low-temperature thermochronometry of apatite, Geochimica et Cosmochimica Acta, 60, 4231–4240, doi:10.1016/S0016-7037(96)00192-5, 1996.

Wolfgramm, M., Bartels, J., Hoffmann, F., Kittl, G., Lenz, G., Seibt, P., Schulz, R., Thomas, R., and Unger, H. J.: Unterhaching geothermal well doublet: structural and hydrodynamic reservoir characteristic; Bavaria (Germany), Proceedings European Geothermal Congress, 2007.

1295 Yanites, B. J., Ehlers, T. A., Becker, J. K., Schnellmann, M., and Heuberger, S.: High magnitude and rapid incision from river capture: Rhine River, Switzerland, J. Geophys. Res. Earth Surf., 118, 1060–1084, doi:10.1002/jgrf.20056, 2013.

Zeitler, P. K., Herczeg, A. L., McDougall, I., and Honda, M.: U-Th-He dating of apatite: A potential thermochronometer, Geochimica et Cosmochimica Acta, 51, 2865–2868, doi:10.1016/0016-7037(87)90164-5, 1987.

Ziegler, P. A.: European Cenozoic rift system, Tectonophysics, 208, 91–111, doi:10.1016/0040-1951(92)90338-7, 1992.

1300 Ziegler, P. A. and Dèzes, P.: Cenozoic uplift of Variscan Massifs in the Alpine foreland: Timing and controlling mechanisms, Global and Planetary Change, 58, 237–269, doi:10.1016/j.gloplacha.2006.12.004, 2007.